Growth and wall-transpiration control of nonlinear unsteady Görtler vortices forced by free-stream vortical disturbances

Elena Marensi*
School of Mathematics and Statistics, The University of Sheffield, Hounsfield Road, S3 7RH Sheffield, United Kingdom

Pierre Ricco
Department of Mechanical Engineering, The University of Sheffield, Mappin Street, S1 3JD Sheffield, United Kingdom

Marensi, E. Ricco, P. Growth and wall-transpiration control of nonlinear unsteady Görtler vortices forced by free-stream vortical disturbances, Accepted in Physics of Fluids

The generation, nonlinear evolution and wall-transpiration control of unsteady Görtler vortices in an incompressible boundary layer over a concave plate is studied theoretically and numerically. Görtler rolls are initiated and driven by free-stream vortical perturbations of which only the low-frequency components are considered because they penetrate the most into the boundary layer. The formation and development of the disturbances are governed by the nonlinear unsteady boundary-region equations with the centrifugal force included. These equations are subject to appropriate initial and outer boundary conditions, which account for the influence of the upstream and free-stream forcing in a rigorous and mutually-consistent manner. Numerical solutions show that the stabilizing effect on nonlinearity, which also occurs in flat-plate boundary layers, is significantly enhanced in the presence of centrifugal forces. Sufficiently downstream the nonlinear vortices excited at different free-stream turbulence intensities Tu saturate at the same level, proving that the initial amplitude of the forcing becomes unimportant. At low Tu the disturbance exhibits a quasi-exponential growth with the growth rate being intensified for more curved plates and for lower frequencies. At higher Tu, in the typical range of turbomachinery applications, the Görtler vortices do not undergo a modal stage as nonlinearity saturates rapidly, and the wall curvature does not affect the boundary-layer response. Good quantitative agreement with data from direct numerical simulations and experiments is obtained. Steady spanwise-uniform and spanwise-modulated zero-mass-flow-rate wall transpiration is shown to attenuate the growth of the Görtler vortices significantly. A novel modified version of the Fukagata-Iwamoto-Kasagi (FIK) identity, used for the first time to study a transitional flow, reveals which terms in the streamwise momentum balance are mostly affected by the wall transpiration, thus offering insight into the increased nonlinear growth of the wall-shear stress.

I. INTRODUCTION

Görtler rolls are streamwise-oriented counter-rotating vortices which develop in boundary layers over concave walls and play a primary role in driving the laminar-to-turbulence transition in many fluid flows of practical importance. In supercritical laminar-flow-control airfoils (i.e., wings that are specially designed to delay the formation of shock waves in the transonic-speed regime), transition may be triggered by centrifugal instability occurring at the leading and trailing edges of the lower surface [31]. In turbomachinery, Görtler vortices increase the heat transfer and the skin friction on the pressure sides of turbine or compressor blades, thus critically affecting the efficiency of the system [26, 54]. As Görtler instability develops in an open domain and is associated with a growing base flow, nonparallel effects and the receptivity to external disturbances are of crucial importance. This was rigorously demonstrated by Hall [21] in 1983. Until then, all analyses neglected the spatial evolution of the boundary layer and resorted to a local eigenmode approach (refer to Saric [43] for an exhaustive review). Instead, Görtler instability must be solved as an initial-value problem [21].

As for other types of boundary-layer instabilities, it is desirable to devise efficient tools to control the amplification of Görtler vortices with the aim of delaying or preventing transition. An even more challenging problem is to include the receptivity analysis in the design of laminar-flow control tools[25]. In this paper, we provide a rigorous mathematical formulation to predict the excitation of unsteady Görtler vortices by free-stream vorticity and their downstream nonlinear amplification. We also investigate the effectiveness of steady wall transpiration for the attenuation of these

* Email: e.marensi@sheffield.ac.uk

boundary-layer disturbances.

Despite experimental evidence of the influence of free-stream vortical disturbances on Görtler instability [5, 27, 50], most of the theoretical and numerical works have so far focused on the excitation of Görtler vortices by other types of external agents, such as surface roughness (e.g. Bassom and Hall [2], Denier et al. [13]) or wall transpiration (e.g. Bertolotti [4], De Souza et al. [12]). These studies, as well as almost the entire available literature on the subject, are devoted to steady vortices because these are the structures primarily observed in a laboratory (a noticeable exception is the experimental and numerical work by Boiko et al. [7], who considered unsteady vortices). However, it has been conjectured that in real transition scenarios, and especially in high turbulence environments which are typical of flows over turbine blades, unsteady Görtler vortices are likely to be at work [47]. Both the influence of free-stream vorticity and the role of unsteadiness are taken into account in the present analysis. The excitation and nonlinear development of the unsteady vortices are described using the rigorous asymptotic approach of the boundary-region equations conceived by Goldstein and co-workers[28, 58]. As opposed to the optimal-growth [11, 30] and the Orr-Sommerfeld [46] approaches, the Goldstein theory consists of the appropriate initial (upstream) and far-field boundary conditions which account for the interaction between the free-stream disturbances and the boundary layer. The reader is referred to the recent work by Ricco et al. [42] for a detailed comparative discussion of these theories. Using the boundary-region approach, Wu et al. [57] investigated the linear development of unsteady Görtler vortices forced by free-stream perturbations and showed that, for curved plates, the streamwise streaks (or Klebanoff modes) may grow exponentially and evolve into Görtler modes further downstream. Ricco et al. [40] studied the nonlinear evolution of laminar streaks in the boundary layer over a flat plate subject to free-stream vorticity. They showed that nonlinearity has a stabilizing effect on the streaks and generates a significant distortion of the mean profile. The problem formulated by Ricco et al. [40] is extended herein to account for centrifugal forces provoked by the concavity of the wall.

A. Nonlinear effects and secondary instability

Görtler vortices themselves do not lead to transition [51]. Instead, due to the upwelling of low-momentum fluid away from the wall and downwelling of high-momentum fluid towards the wall (i.e., the so-called lift-up effect), elongated low-speed and high-speed regions are generated between the vortices, which results in highly distorted velocity profiles. Further downstream, these low-high momentum distributions yield mushroom-like structures of the streamwise velocity iso-contours in cross-flow planes. Swearingen and Blackwelder [51] identified two types of secondary-instability modes responsible for the laminar breakdown: sinuous modes, driven by unstable inflectional spanwise profiles, and varicose modes, associated with instability in the inflectional normal profiles. The former was found to be the most preferred mechanism of transition (refer also to the experiments of Tandiono et al. [52, 53]).

The nonlinear development of steady Görtler vortices was studied numerically by Hall [22, 23], Benmalek and Saric [3] and Souza [49]. After a relatively short linear regime, the disturbance energy was found to saturate and highly-distorted profiles were detected. The existence of sinuous and varicose modes was confirmed by secondary instability calculations [e.g. 24, 29], which clarified the relative importance of these two types of instability in the transition process. All these calculations were performed for steady Görtler vortices. In their DNS of unsteady Görtler flow induced by broadband free-stream turbulence, Schrader et al. [46] showed that the transition process over a curved plate is similar to that occurring over a flat plate, although in the latter case the breakdown to turbulence occurred further downstream than in a Görtler flow.

B. Control via wall transpiration

The use of wall transpiration as a flow-control technique in flat-plate boundary layers has been widely studied and is known to be effective in attenuating the growth of pre-transitional disturbances such as Klebanoff modes (refer for examples to the experiments of Yoshioka et al. [59] and to the theoretical studies based on the boundary-region approach by Ricco and Dilib [39] and Ricco et al. [41]) and Tollmien-Schlichting (T-S) waves [6]. The effect of suction on the Görtler instability is instead still a relatively unexplored subject. Floryan and Saric [18] formulated a stability analysis using self-similar suction profiles as a base flow and found that Görtler vortices are stabilized in both cases, although a larger level of suction is required as compared to the T-S wave case. Myose and Blackwelder [33] performed a series of experiments introducing localized suction slots underneath the low-speed regions between counter-rotating vortex pairs and showed that a much lower level of suction was required to delay the laminar breakdown with this method as compared to an asymptotic suction profile approach. However, the high levels of suction rate created an additional spanwise instability which led to premature transition. Optimal control techniques were employed by Balakumar and Hall [1], Cathalifaud and Luchini [10] and Papadakis et al. [34] to determine the optimal distribution

of the wall transpiration to minimize the growth rate of boundary layer disturbances under certain constraints on the suction and blowing amplitude. They were able to achieve a significant attenuation of the disturbance energy using either suction or blowing of small amplitude. A proportional control algorithm was developed by Sescu et al. [48] to control Görtler instabilities by means of wall deformations or wall transpiration. The former method was found to be more efficient in minimizing the energy associated with the unsteady Gö rtler vortices. Steady spanwise-uniform and spanwise-modulated zero-mass-flow-rate wall transpiration is used in the present analysis to attenuate the growth of Görtler vortices.

C. Objectives

The first goal of the present work is to predict, through a rigorous mathematical formulation, the generation of unsteady Görtler vortices by free-stream vortical disturbances, their downstream amplification and nonlinear evolution. Although the nonlinear evolution of Görtler vortices has been investigated by a number of researchers [e.g. 3, 22], these works are concerned with steady vortices. A further objective is to attenuate the growth of the nonlinear vortices by steady wall transpiration. We also analyze the change of wall friction through a modified version of the Fukagata-Iwamoto-Kasagi (FIK) identity [19], which is typically used to study fully-developed turbulent flows. This novel integral relation is employed on a transitional flow for the first time.

It should be noted that, during the final stages of writing, results on the excitation of Görtler vortices by free-stream vorticity have been published [14, 15]. Although Dongdong et al. [14]'s mathematical formulation is very similar to ours, an important difference resides in our paper presenting wall-based control results, while Dongdong et al. [14]'s work focusing on the secondary instability of the vortices. Dongdong et al. [14] mainly study steady Görtler vortices, whereas our main objective has been to characterize the unsteady nonlinear Görtler instability thoroughly by carrying out a complete parametric study. Furthermore, our chosen set of experimental data used for comparison is different from Dongdong et al. [14]'s and, for the first time our study employs a variant of the FIK identity to investigate a transitional boundary layer. A distinct feature of our integral identity with respect to the analogous equation for open turbulent boundary layers, derived in the original FIK publication[19], is the use of the asymptotically large upper limit of the integral along the wall-normal direction, which simplifies the relation and renders it more general. In the original FIK identity for free-stream wall-bounded flows this upper limit is instead fixed to the boundary-layer thickness.

II. MATHEMATICAL FORMULATION AND NUMERICAL PROCEDURES

An incompressible boundary-layer flow over a longitudinally concave wall with constant radius of curvature r_0^* is considered (hereinafter the superscript * indicates dimensional quantities). The boundary layer is generated by a uniform flow of velocity U_∞^* perturbed by unsteady convected-gust vortical fluctuations encountering the infinitely thin curved plate. Spanwise-uniform and spanwise-distributed wall transpiration is applied to inhibit the boundary-layer disturbances. Figure 1 shows a schematic of the flow domain.

The flow is described in an orthogonal curvilinear coordinate system $\{x^*, y^*, z^*\}$, where x^*, y^* and z^* represent the streamwise, wall-normal, and spanwise coordinates, respectively. The problem is formulated by introducing a suitable reference length scale λ^*, which we shall define below, and by scaling the velocity components by U_∞^*. The time t^* and the pressure p^* are scaled by λ^*/U_∞^* and $\rho^* U_\infty^{*2}$, respectively, where ρ^* is the density of the fluid.

Although free-stream turbulence should, in general, be modeled as a continuous spectrum of modes [60], we consider the simplified case where the boundary layer is forced only by a pair of vortical modes. Following Ricco et al. [40], the forcing modes are characterized by the same frequency f^* (and hence streamwise wavenumber k_x^*), but opposite spanwise wavenumber $\pm k_z^*$. The free-stream disturbance $\mathbf{u}_\infty^*$ is passively advected by U_∞^* and is written as

$$\mathbf{u}_\infty(x-t,y,z) = \epsilon\left(\hat{\mathbf{u}}_+^\infty e^{ik_z z} + \hat{\mathbf{u}}_-^\infty e^{-ik_z z}\right) e^{ik_x(x-t)+ik_y y} + c.c.,$$

where $\hat{\mathbf{u}}_\pm^\infty = \{\hat{u}_{x,\pm}^\infty, \hat{u}_{y,\pm}^\infty, \hat{u}_{z,\pm}^\infty\} = \mathcal{O}(1)$, $\epsilon \ll 1$ indicates the amplitude of the oncoming disturbance, and *c.c.* denotes the complex conjugate. The continuity equation must be satisfied in the free stream, i.e.

$$k_x \hat{u}_{x,\pm}^\infty + k_y \hat{u}_{y,\pm}^\infty \pm k_z \hat{u}_{z,\pm}^\infty = 0. \tag{1}$$

A convenient choice for the reference length scale is $\lambda^* = \lambda_z^*/(2\pi) = 1/k_z^*$ [32], where λ_z^* is the spanwise wavelength of the free-stream perturbation. It follows that $k_z = 1$, but, for clarity, the dependence on k_z will be expressed explicitly henceforth. The Reynolds number is defined as $R_\lambda \equiv U_\infty^* \lambda^*/\nu^* \gg 1$, where ν^* is the kinematic viscosity of the fluid.

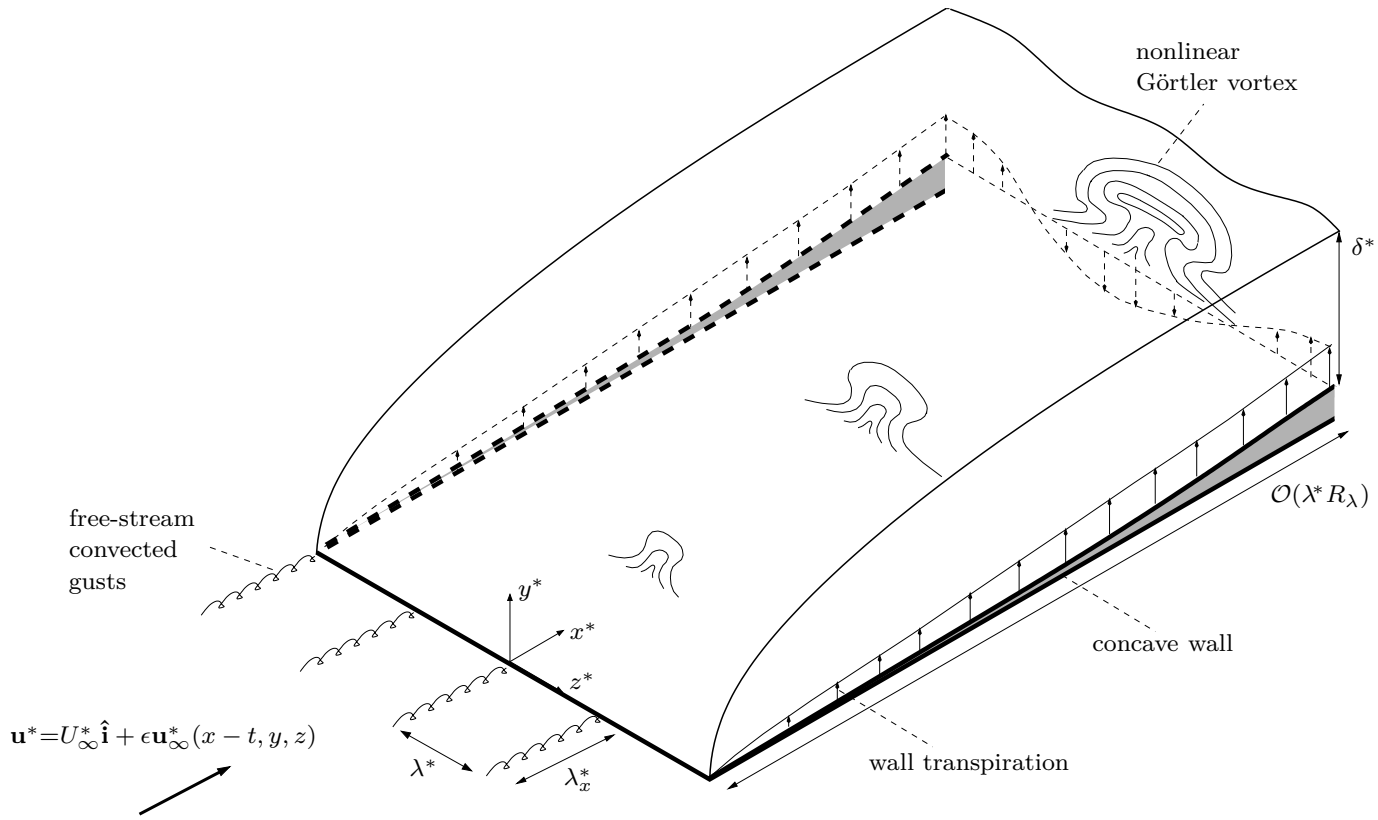

FIG. 1. Sketch of the flow domain for a case of steady spanwise-modulated wall transpiration.

Attention is focused on the components of the free-stream perturbation with long streamwise wavelengths $\lambda^*_x \gg \lambda^*_z$, that is $k_x \ll 1$. In the flat plate case, experiments have confirmed that these low-frequency components can penetrate into the boundary layer to generate Klebanoff modes. Wu et al. [57] showed that Klebanoff modes over concave plates may develop into Görtler vortices at $x^*{=}\mathcal{O}(\lambda^*_x)$ after reaching their maximum amplitude. Therefore, the slow streamwise distance $\bar{x}{=}k_x x{=}\mathcal{O}(1)$ and the slow time $\bar{t}{=}k_x t{=}\mathcal{O}(1)$ are introduced. The local boundary-layer thickness δ^* becomes comparable with λ^* when $x{=}\mathcal{O}(R_\lambda)$. At these locations viscous diffusion effects in the spanwise and wall-normal directions are comparable. As $\bar{x}{=}\mathcal{O}(1)$, it follows that $k_x R_\lambda{=}\mathcal{O}(1)$, or, equivalently, $\kappa_z{\equiv}k_z/\sqrt{k_x R_\lambda}{=}\mathcal{O}(1)$.

A. Governing equations

We derive the governing equations from the full incompressible Navier-Stokes equations written in curvilinear coordinates with Lamé coefficients [17] $h_1{=}(r_0{-}y)/r_0$, $h_2{=}h_3{=}1$. The velocity field is rescaled as $\{u,v,w\}{=}\{\tilde{u},\sqrt{k_x/R_\lambda}\tilde{v},k_x\tilde{w}\}$ and the pressure as $p{=}k_x\tilde{p}/R_\lambda$. By performing the change of variable $(x,t){\to}(\bar{x},\bar{t})$ and taking the limits $k_x^{-1},R_\lambda{\to}\infty$ with $k_x R_\lambda{=}\mathcal{O}(1)$, we obtain the following leading-order equations

$$\frac{\partial\tilde{u}}{\partial\bar{x}} + \frac{\kappa_z}{k_z}\frac{\partial\tilde{v}}{\partial y} + \frac{\partial\tilde{w}}{\partial z} = 0, \tag{2a}$$

$$\frac{\partial\tilde{u}}{\partial\bar{t}} + \tilde{u}\frac{\partial\tilde{u}}{\partial\bar{x}} + \frac{\kappa_z}{k_z}\tilde{v}\frac{\partial\tilde{u}}{\partial y} + \tilde{w}\frac{\partial\tilde{u}}{\partial z} = \frac{\kappa_z^2}{k_z^2}\left(\frac{\partial^2\tilde{u}}{\partial y^2} + \frac{\partial^2\tilde{u}}{\partial z^2}\right), \tag{2b}$$

$$\frac{\partial\tilde{v}}{\partial\bar{t}} + \tilde{u}\frac{\partial\tilde{v}}{\partial\bar{x}} + \frac{\kappa_z}{k_z}\tilde{v}\frac{\partial\tilde{v}}{\partial y} + \tilde{w}\frac{\partial\tilde{v}}{\partial z} + \mathcal{G}\tilde{u}^2 = \frac{\kappa_z^2}{k_z^2}\left(-\frac{\partial\tilde{p}}{\partial y} + \frac{\partial^2\tilde{v}}{\partial y^2} + \frac{\partial^2\tilde{v}}{\partial z^2}\right), \tag{2c}$$

$$\frac{\partial\tilde{w}}{\partial\bar{t}} + \tilde{u}\frac{\partial\tilde{w}}{\partial\bar{x}} + \frac{\kappa_z}{k_z}\tilde{v}\frac{\partial\tilde{w}}{\partial y} + \tilde{w}\frac{\partial\tilde{w}}{\partial z} = \frac{\kappa_z^2}{k_z^2}\left(-\frac{\partial\tilde{p}}{\partial z} + \frac{\partial^2\tilde{w}}{\partial y^2} + \frac{\partial^2\tilde{w}}{\partial z^2}\right), \tag{2d}$$

where

$$\mathcal{G} \equiv \frac{R_\lambda^{1/2}}{k_x^{3/2} r_0} = \mathcal{O}(1) \tag{3}$$

is the Görtler number, which accounts for the centrifugal effects. he Görtler number is well defined as we only consider unsteady disturbances ($k_x \neq 0$). The radius of curvature r_0^* is assumed to be much larger than the spanwise wavelength λ_z^*, i.e., $r_0 = \mathcal{O}\left(R_\lambda^{1/2}/k_x^{3/2}\right) \gg 1$. We express the boundary-layer solution as a superimposition of the disturbance generated by the free-stream perturbation onto the Blasius flow, namely

$$\begin{aligned}\{\tilde{u}, \tilde{v}, \tilde{w}, \tilde{p}\} = \left\{F', \frac{\eta F' - F}{\sqrt{2\bar{x}}}, 0, -\frac{1}{2}\right\} + r_t \Big\{ & \bar{u}\left(\bar{x}, \eta, z, \bar{t}\right), \sqrt{2\bar{x}}\bar{v}\left(\bar{x}, \eta, z, \bar{t}\right), \\ & k_z^{-1}\bar{w}\left(\bar{x}, \eta, z, \bar{t}\right), \bar{p}\left(\bar{x}, \eta, z, \bar{t}\right)\Big\},\end{aligned} \tag{4}$$

where $F(\eta)$ is the Blasius solution [40], $\eta \equiv y\sqrt{k_x R_\lambda / 2\bar{x}}$ is the similarity variable, and $r_t \equiv \epsilon R_\lambda = \mathcal{O}(1)$ is the turbulent Reynolds number. Unless otherwise specified, henceforth the prime indicates the derivative with respect to η. The disturbance is expressed as a Fourier series in time and z,

$$\{\bar{u}, \bar{v}, \bar{w}, \bar{p}\} = \sum_{m,n=-\infty}^{\infty} \{\hat{u}_{m,n}, \hat{v}_{m,n}, \hat{w}_{m,n}, \hat{p}_{m,n}\} \, e^{im\bar{t} + ink_z z}, \tag{5}$$

where $\{\hat{u}_{m,n}, \hat{v}_{m,n}, \hat{w}_{m,n}, \hat{p}_{m,n}\}$ are functions of $\bar{x}$ and η. As $\{\bar{u}, \bar{v}, \bar{w}, \bar{p}\}$ are real, the Hermitian property applies to the Fourier coefficients, i.e., $\hat{u}_{m,n} = \hat{u}^\star_{-m,-n}$, where the superscript * indicates the complex conjugate. By substituting (4) and (5) into (2) and using the change of variable $(\bar{x}, y) \to (\bar{x}, \eta(\bar{x}, y))$ the nonlinear boundary-region equations are derived as

Continuity

$$\frac{\partial \hat{u}_{m,n}}{\partial \bar{x}} - \frac{\eta}{2\bar{x}}\frac{\partial \hat{u}_{m,n}}{\partial \eta} + \frac{\partial \hat{v}_{m,n}}{\partial \eta} + in\hat{w}_{m,n} = 0, \tag{6}$$

x-Momentum

$$\left(im - \frac{\eta F''}{2\bar{x}} + \kappa_z^2 n^2\right)\hat{u}_{m,n} + F'\frac{\partial \hat{u}_{m,n}}{\partial \bar{x}} - \frac{F}{2\bar{x}}\frac{\partial \hat{u}_{m,n}}{\partial \eta} - \frac{1}{2\bar{x}}\frac{\partial^2 \hat{u}_{m,n}}{\partial \eta^2} + F''\hat{v}_{m,n} = r_t\hat{\mathcal{X}}_{m,n}, \tag{7}$$

y-Momentum

$$\begin{aligned}&\left(\frac{F - \eta F' - \eta^2 F''}{4\bar{x}^2} + \frac{2\mathcal{G}F'}{\sqrt{2\bar{x}}}\right)\hat{u}_{m,n} + \left(im + \frac{\eta F''}{2\bar{x}} + \frac{F'}{2\bar{x}} + \kappa_z^2 n^2\right)\hat{v}_{m,n} + F'\frac{\partial \hat{v}_{m,n}}{\partial \bar{x}} \\ &- \frac{F}{2\bar{x}}\frac{\partial \hat{v}_{m,n}}{\partial \eta} - \frac{1}{2\bar{x}}\frac{\partial^2 \hat{v}_{m,n}}{\partial \eta^2} + \frac{1}{2\bar{x}}\frac{\partial \hat{p}_{m,n}}{\partial \eta} = r_t\hat{\mathcal{Y}}_{m,n},\end{aligned} \tag{8}$$

z-Momentum

$$\left(im + n^2\kappa_z^2\right)\hat{w}_{m,n} + F'\frac{\partial \hat{w}_{m,n}}{\partial \bar{x}} - \frac{F}{2\bar{x}}\frac{\partial \hat{w}_{m,n}}{\partial \eta} - \frac{1}{2\bar{x}}\frac{\partial^2 \hat{w}_{m,n}}{\partial \eta^2} + in\kappa_z^2\hat{p}_{m,n} = r_t\hat{\mathcal{Z}}_{m,n}, \tag{9}$$

where $\hat{\mathcal{X}}_{m,n}$, $\hat{\mathcal{Y}}_{m,n}$ and $\hat{\mathcal{Z}}_{m,n}$ represent the nonlinear terms

$$\hat{\mathcal{X}}_{m,n} = \left[-\frac{\partial \widehat{\bar{u}\bar{u}}}{\partial \bar{x}} + \frac{\eta}{2\bar{x}} \frac{\partial \widehat{\bar{u}\bar{u}}}{\partial \eta} - \frac{\partial \widehat{\bar{u}\bar{v}}}{\partial \eta} - ni\widehat{\bar{u}\bar{w}} \right]_{m,n},$$

$$\hat{\mathcal{Y}}_{m,n} = \left[-\frac{\widehat{\bar{u}\bar{v}}}{2\bar{x}} - \frac{\partial \widehat{\bar{u}\bar{v}}}{\partial \bar{x}} + \frac{\eta}{2\bar{x}} \frac{\partial \widehat{\bar{u}\bar{v}}}{\partial \eta} - \frac{\partial \widehat{\bar{v}\bar{v}}}{\partial \eta} - ni\widehat{\bar{v}\bar{w}} - \frac{\mathcal{G}}{\sqrt{2\bar{x}}}\widehat{\bar{u}\bar{u}} \right]_{m,n},$$

$$\hat{\mathcal{Z}}_{m,n} = \left[-\frac{\partial \widehat{\bar{u}\bar{w}}}{\partial \bar{x}} + \frac{\eta}{2\bar{x}} \frac{\partial \widehat{\bar{u}\bar{w}}}{\partial \eta} - \frac{\partial \widehat{\bar{v}\bar{w}}}{\partial \eta} - ni\widehat{\bar{w}\bar{w}} \right]_{m,n}.$$

In the limit $\mathcal{G}\to 0$, the nonlinear unsteady boundary-region equations of Ricco et al. [40] are recovered. By rescaling the velocity and pressure fields as:

$$\{\bar{u}, \bar{v}, \bar{w}, \bar{p}\} = \left\{ u^\dagger(\hat{x}, \eta), \hat{k}_x^{-1} v^\dagger(\hat{x}, \eta), \hat{k}_x^{-1} w^\dagger(\hat{x}, \eta), \hat{k}_x^{-1} p^\dagger(\hat{x}, \eta) \right\}, \tag{11}$$

where $\hat{k}_x = k_x R_\lambda$ and $\hat{x} = \bar{x}/\hat{k}_x = x/R_\lambda$, the linear parts of (6)-(9) can be recast into equations (2.15)-(2.18) of Wu et al. [57] and the definition of Görtler number adopted by Wu et al. [57], i.e., $G_\lambda = R_\lambda^2/r_0 = \mathcal{O}(1)$, is found.

B. The upstream, free-stream, and wall boundary conditions

Appropriate upstream, free-stream (outer), and wall boundary conditions are needed to solve the equations (6)-(9). The outer boundary conditions are derived by matching the boundary-layer solution with the free-stream solution as $\eta\to\infty$. At $\bar{x} = \mathcal{O}(1)$ the outer flow is influenced at the leading order by the displacement effect due to the presence of the viscous layer. In addition to the three-dimensional vortical gust advected from upstream, the disturbance in the outer region includes a two-dimensional irrotational perturbation. The latter is induced by the additional displacement effect due to the nonlinear boundary-layer interactions. As in Ricco et al. [40], far from the plate the streamwise velocity component does not force the boundary-layer perturbations at leading order and therefore $\hat{u}_{m,n}\to 0$ as $\eta\to\infty$. It follows that the centrifugal effects are negligible in the free stream because the terms containing $\mathcal{G}$ in equation (8) are proportional to the streamwise velocity. The outer boundary conditions are thus the same as those in Ricco et al. [40], namely

$$\{\hat{u}_{m,n}, \hat{v}_{m,n}, \hat{w}_{m,n}, \hat{p}_{m,n}\} \to \left\{ 0, \frac{\kappa_z}{k_z\sqrt{2\bar{x}}} v^\dagger_{m,n}, \frac{\kappa_z^2}{k_z} w^\dagger_{m,n}, \boldsymbol{r_t} \left(\frac{\boldsymbol{\kappa_z}}{\boldsymbol{k_z}}\right)^{\mathbf{2}} p^\dagger_{m,n} \right\} \tag{12}$$

as $\eta\to\infty$ for $\bar{x} = \mathcal{O}(1)$, with

$$v^\dagger_{m,\pm1} = -\frac{\kappa_z}{\kappa_y} e^{-(\kappa_y^2+\kappa_z^2)\bar{x}} \left[\hat{\phi}_m e^{-i(\bar{x}+\kappa_y\sqrt{2\bar{x}}\eta)} + \hat{\phi}^\star_{-m} e^{i(\bar{x}+\kappa_y\sqrt{2\bar{x}}\eta)} \right],$$

$$w^\dagger_{m,\pm1} = \pm e^{-(\kappa_y^2+\kappa_z^2)\bar{x}} \left[\hat{\phi}_m e^{-i(\bar{x}+\kappa_y\sqrt{2\bar{x}}\eta)} - \hat{\phi}^\star_{-m} e^{i(\bar{x}+\kappa_y\sqrt{2\bar{x}}\eta)} \right],$$

$$p^\dagger_{0,\pm2} = 2e^{-2(\kappa_y^2+\kappa_z^2)\bar{x}},$$

$$p^\dagger_{m,0} = -\frac{2\kappa_z^2}{\kappa_y^2} e^{-2(\kappa_y^2+\kappa_z^2)\bar{x}} \left[\hat{\pi}_m e^{-2i(\bar{x}+\kappa_y\sqrt{2\bar{x}}\eta)} + \hat{\pi}^\star_{-m} e^{2i(\bar{x}+\kappa_y\sqrt{2\bar{x}}\eta)} \right],$$

where $\kappa_y \equiv k_y/\sqrt{k_x R_\lambda} = \mathcal{O}(1)$, $v^\dagger_{m,n} = w^\dagger_{m,n} = 0$ if $n \neq \pm 1$, and $p^\dagger_{m,n} = 0$ if $n \neq 0, \pm 2$. The coefficients $\hat{\phi}_m$ and $\hat{\pi}_m$ are found in Ricco et al. [40] (refer to their equation (2.26)) and depend on the boundary-layer displacement thickness. The condition on $\hat{v}_{m,n}$ in (12) is valid only when $n \neq 0$. In the spanwise-averaged case ($n=0$) the pressure only appears in the y-momentum equation and the velocity components are thus calculated by only solving the continuity, x- and z-momentum equations (refer also to Marensi [32] on page 56).

The equations (6)-(9) are parabolic in the streamwise direction and are subject to initial conditions for $\bar{x}\to 0$. Since $\bar{u}\to 0$ as $\bar{x}\to 0$, the centrifugal terms are negligible in this limit. The velocity fluctuations are thus of small amplitude

and evolve linearly near the leading edge. Therefore, we recover the initial conditions of Leib et al. [28], namely

$$\{\hat{u},\hat{v},\hat{w},\hat{p}\}_{-1,\pm1} \rightarrow \frac{i\kappa_z^2}{k_z}\left(\pm\hat{u}^{\infty}_{z,\pm}+\frac{ik_z}{\sqrt{k_x^2+k_z^2}}\hat{u}^{\infty}_{y,\pm}\right)\{U_{in},V_{in},\mp iW_{in}\} \tag{14}$$

as $\bar{x}\rightarrow 0$, where $\{U_{in},V_{in},W_{in}\}$ are given by the right-hand sides of equations (5.25)-(5.27) in Leib et al. [28]. The velocity fluctuations of all the other harmonics generated by the nonlinear interactions are imposed to vanish upstream. The same upstream conditions have been employed in the linear case of Wu et al. [57].

Steady wall transpiration is applied on the spanwise-averaged mode and on the first four spanwise harmonics, namely $\hat{v}_{0,n}(\eta{=}0){=}A_w$, where $n{\in}\mathbb{Z}{=}0{\leq}n{\leq}4$, and A_w is the amplitude of the wall transpiration. Note that the physical amplitude of the wall-transpiration grows with $\sqrt{2\bar{x}}$ because of the definition of wall-normal velocity adopted in (4). The no-slip condition is imposed on the wall-normal velocity component of the other modes and on the streamwise and spanwise velocity components. Our wall-based forcing strategy bears analogy with the method devised experimentally by Saric et al. [44, 45] and studied numerically by Wassermann and Kloker [55] to delay the downstream occurrence of the secondary instability of cross-flow vortices. Small artificial roughness elements are placed near the leading edge to trigger steady spanwise-modulated vortices with a spanwise wavelength which is shorter than the one of the fundamental mode, similarly to our case for modes with $n = 2, 3, 4$. The main difference is that our control approach is active as energy is fed into the system, while the method of Saric and co-workers[44, 45] is passive as it involves a geometrical modification.

C. Integral relation for the wall-shear stress

In this section, we present an explicit relation between the increase of the wall-shear stress due to nonlinear effects and wall-normal integrals of terms appearing in the streamwise momentum equation (7). This equation is obtained by following the procedure first proposed by Fukagata et al. [19], whose identity has been used widely to investigate how the turbulent skin-friction coefficient can be modified by manipulation of the Reynolds stresses. In our Görtler-flow case, the increase of wall-shear stress with respect to the Blasius nominal value is expressed as follows:

$$\begin{aligned}\tau_w^{0,0}(\bar{x}) &\equiv \left.\frac{\partial\hat{u}_{0,0}}{\partial\eta}\right|_{\eta=0} \equiv \sum_{i=1}^{5}\widetilde{\mathcal{M}_i} \equiv \sum_{i=1}^{5}\int_0^{\infty}\mathcal{M}_i\mathrm{d}\eta = \\ &= \int_0^{\infty}\Bigg[\underbrace{(\eta F''-F')\,\hat{u}_{0,0}}_{\mathcal{M}_1}\underbrace{-2\bar{x}F'\frac{\partial\hat{u}_{0,0}}{\partial\bar{x}}}_{\mathcal{M}_2}\underbrace{-2\bar{x}F''\hat{v}_{0,0}}_{\mathcal{M}_3}\underbrace{-2\bar{x}r_t\left.\frac{\partial\widehat{\overline{uu}}}{\partial\bar{x}}\right|_{0,0}}_{\mathcal{M}_4}\underbrace{-r_t\left.\widehat{\overline{uu}}\right|_{0,0}}_{\mathcal{M}_5}\Bigg]\mathrm{d}\eta.\end{aligned} \tag{15}$$

Two important differences between (15) and equation (15) in Fukagata et al. [19] can be noted. The upper limit of the integral (15) is arbitrarily large and therefore the identity is not linked to any specific definition of the boundary-layer thickness, while Fukagata et al. [19]'s integration extends to $y^* = \delta^*_{99}$, i.e., to the wall-normal location where the mean streamwise velocity equals $0.99U^*_{\infty}$. Furthermore, the Reynolds stresses $\widehat{\overline{uv}}|_{0,0}$ vanish in our case, whereas they appear in Fukagata et al. [19]'s equations for both confined turbulent channel flows and open turbulent boundary layers. The derivation of relation (15) is found in the Appendix.

D. Numerical procedures

A detailed description of the numerical procedure is found in Marensi [32]. The equations (6)-(9) with far-field boundary conditions (12) and initial conditions (14) are solved by a marching procedure in $\bar{x}$, which is based on a second-order finite-difference scheme. The typical grid sizes in the wall-normal and streamwise directions are $\Delta\eta{=}0.03$ and $\Delta\bar{x}{=}0.01$ and the wall-normal domain extends to $\eta_{max}{=}60$. A predictor-corrector algorithm is employed to integrate the nonlinear equations, where the nonlinear terms are calculated at each iteration using the pseudo-spectral method [9]. A number of modes, $N_t{=}N_z{=}37$, is needed to capture the nonlinear effects. Careful resolution checks have been carried out to verify that the spectral truncation does not affect the flow dynamics. Due to the rapid growth of the Görtler vortices, under-relaxation is employed to aid the convergence of the algorithm[37]. Depending on r_t, an under-relaxation factor between 0.6 and 0.8 is chosen. In the linearized case the code has been validated against the results of Wu et al. [57] (refer to Appendix E in Marensi [32]).

The initial conditions (14) for the wall-normal and spanwise velocity components contain a term proportional to $\exp\left[-|\kappa_z|(2\bar{x})^{1/2}\eta\right]$, which represents a disturbance reflected by the wall. The mixed boundary conditions (5.28)-(5.31) of Leib et al. [28] accommodate the wall-normal decay of this reflected disturbance. The Dirichlet conditions (12) are consistent with the initial conditions (14) if $|\kappa_z|(2\bar{x})^{1/2}\eta \gg 1$, i.e., when the reflected disturbance is negligible. A switch between mixed and Dirichlet boundary conditions in the numerical solution assures that the overlapping condition $\eta \gg 1/\left[|\kappa_z|(2\bar{x})^{1/2}\right]$ is satisfied at small $\bar{x}$ without the need of an excessively large η_{max} [40]. In Appendix D of Marensi [32] the far-field conditions derived by Leib et al. [28] and Ricco et al. [40] are shown to be consistent as they both match asymptotically onto the oncoming free-stream disturbance.

III. RESULTS

We select the flow parameters for our numerical simulations to correspond to those in the experiments of Boiko et al. [7] (refer to table I). Unless otherwise stated, $\hat{u}^{\infty}_{x,\pm}=\hat{u}^{\infty}_{y,\pm}=1$ and $\hat{u}^{\infty}_{z,\pm}=\mp 1$. The continuity relation (1) thus becomes $k_x + k_y = 1$ and the turbulence level, defined as the root mean square (r.m.s. hereinafter) of the free-stream streamwise velocity, is $Tu(\%)=100\times 2\epsilon\sqrt{(\hat{u}^{\infty}_{x,+})^2+(\hat{u}^{\infty}_{x,-})^2}=100\times 2\sqrt{2}\epsilon$. Boiko et al. [7] carried out their experiments at very low disturbance levels to guarantee a linear dynamics. We start from this weak free-stream disturbance case and gradually increase $Tu(\%)$ to investigate the nonlinear dynamics of the unsteady Görtler vortices.

Case	U^*_∞ [ms^{-1}]	λ^*_z [m] $\times 10^3$	r^*_0 [m]	f^* [Hz]	λ^*_x [m]	R_λ	G_λ	$\hat{k}_x$	k_x $\times 10^3$	κ_z	$\mathcal{G}$
1	9.18	8	8.37	5	1.84	767	89.5	3.336	4.35	0.547	14.7
2	9.18	8	8.37	11	0.83	767	89.5	7.342	9.57	0.369	4.5

TABLE I. Parameters from the experiments of Boiko et al. [7]. The selected cases correspond to $F_b \equiv 2\pi f^*\nu^*/U^{*2}_\infty \times 10^6 = 5.67$ (case 1) and 12.48 (case 2) in Boiko et al. [7].

A. Effect of turbulence level

The intensity of the boundary-layer perturbation is measured by the r.m.s. of the streamwise velocity disturbance, defined as [36]:

$$u_{rms} \equiv r_t \sqrt{\sum_{m=-\bar{N}_t}^{\bar{N}_t} \sum_{n=-\bar{N}_z}^{\bar{N}_z} |\hat{u}_{m,n}|^2}, \quad m \neq 0,$$

where $\bar{N}_{t,z}=(N_{t,z}-1)/2$. Figure 2 (left) shows the downstream evolution of $u_{rms,max}(\bar{x}) \equiv \max_\eta u_{rms}(\bar{x},\eta)$ for the parameters of case 1 at low free-stream turbulence intensities, i.e., r_t=0.001, 0.01, 0.1. The nonlinear solutions and the corresponding linearized solutions overlap for a significant downstream distance from the leading edge. Görtler vortices undergo exponential growth during their linear development. Due to the intense amplification of the perturbation, nonlinearity comes into play abruptly to inhibit the velocity fluctuations and to cause a sharp deviation of the nonlinear solutions from the linear ones. These effects are enhanced for higher turbulence Reynolds numbers. The stabilizing effect of nonlinearity was already noticed by Ricco et al. [40] for Klebanoff modes developing over a flat plate and by Hall [22] for steady Görtler vortices over a concave wall. Sufficiently downstream the nonlinear solutions generated at different r_t saturate at the same amplitude, decreasing very slowly. Hall [22] conjectured that, since the effective spanwise wavenumber is large at a large distance from the leading edge, the small-wavelength asymptotic theory of Hall [20] holds, i.e., there exists a unique solution, independent of the initial amplitude of the perturbation. This behavior was not observed in the flat-plate case of Ricco et al. [40].

The downstream evolution of the wall-normal position $\eta_{rms,max}$, i.e., the location where the maximum of the streamwise velocity r.m.s. occurs, is displayed in figure 2 (right). In the linear case $\eta_{rms,max}$ decreases monotonically from 1.64 as the streamwise distance increases. At downstream locations where nonlinearity first exerts its influence, a rapid shift of $\eta_{rms,max}$ towards the free stream is observed. At downstream locations where the intensity of the

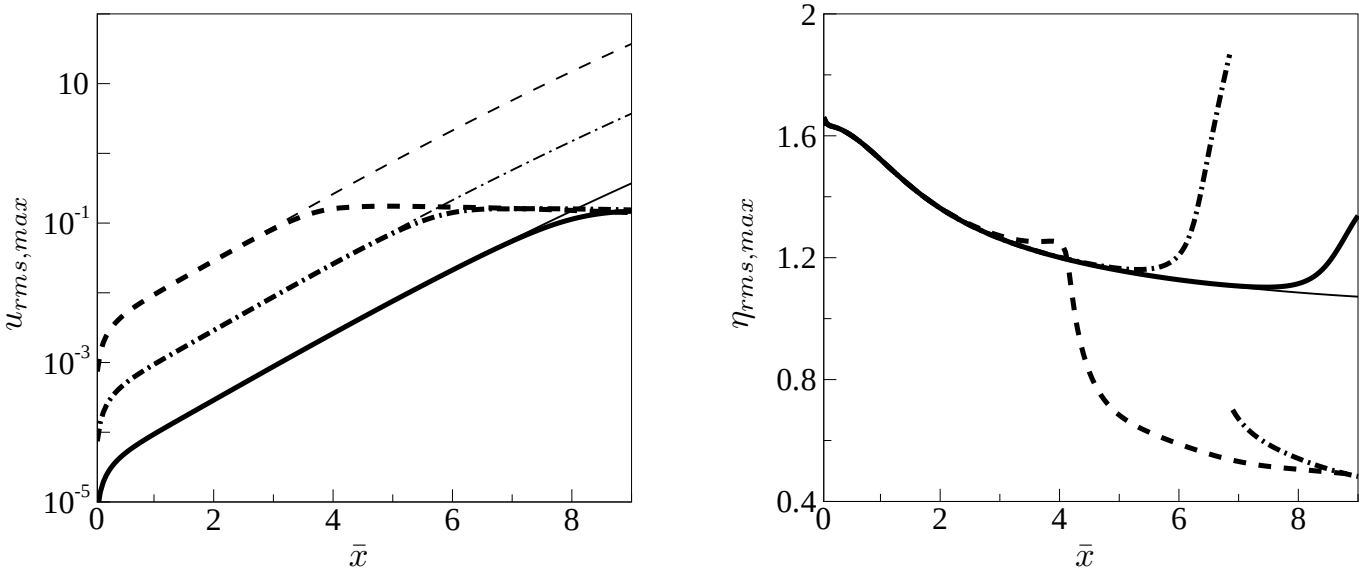

FIG. 2. Effect of low free-stream turbulence intensity on the downstream development of $u_{rms-max}$ (left) and its associated wall-normal peak $\eta_{rms,max}$ (right): r_t=0.001 (solid line), 0.01 (dash-dotted line), 0.1 (dashed line) for $\mathcal{G}$=14.7 and k_x=0.00435 (refer to case 1 in table I). The thin/thick curves indicate the linearized/nonlinear solutions. In the right graph, the discontinuity of the curve for the case r_t=0.01 (dash-dotted line) is due to the presence of two peaks in the wall-normal profile of the $u_{rms-max}$.

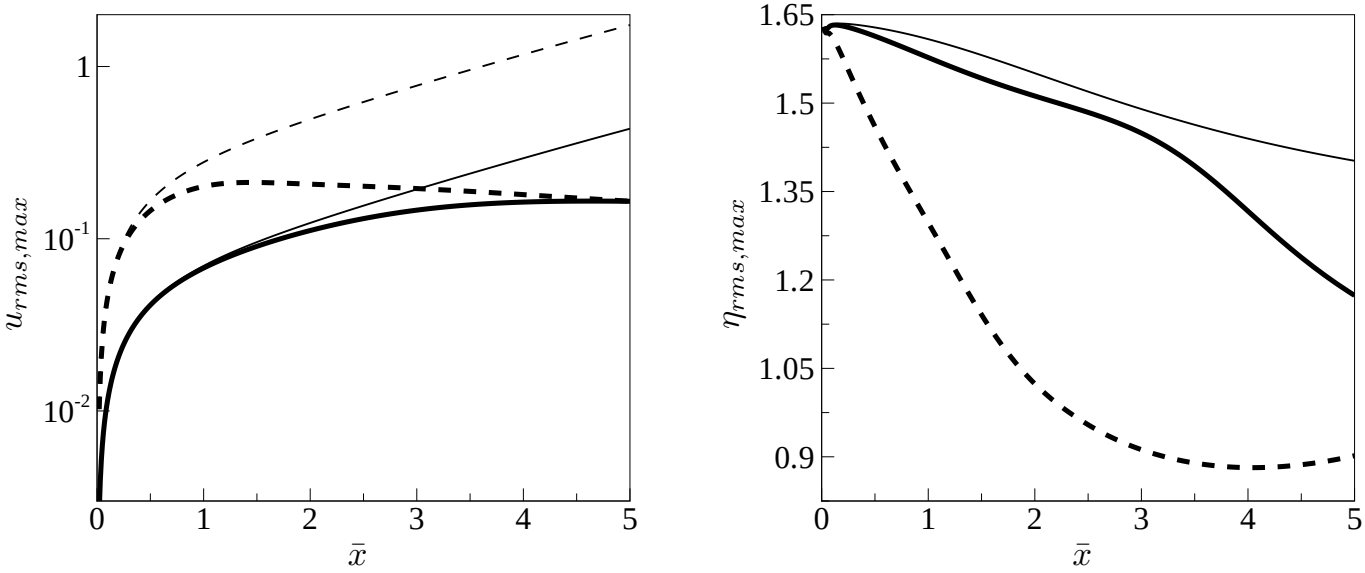

FIG. 3. Effect of high free-stream turbulence intensity on the downstream development of $u_{rms-max}$ (left) and its associated wall-normal peak $\eta_{rms,max}$ (right): r_t=1.34 (solid line) and r_t=5.36 (dashed line) for $\mathcal{G}$=4.5 and k_x=0.00957 (refer to case 2 in table I). The thin/thick curves indicate the linearized/nonlinear solutions.

Görtler vortices is independent of the free-stream forcing amplitude, $\eta_{rms,max}$ decreases to approximately 0.5. Therefore the saturated boundary-layer perturbations concentrate in a region close to the wall. This rapid wallward shift of the vortices is not observed in other nonlinear analyses of either unsteady laminar streaks [40] or steady Görtler vortices [22].

We now turn our attention to free-stream perturbations with r_t>1, i.e., at least one order of magnitude more intense than the largest r_t case in figure 2. The range of $Tu(\%)$ is typical of turbomachinery systems. The other parameters correspond to case 2 in table I. Figure 3 (left) shows the downstream amplification of $u_{rms-max}$ for Tu=0.5% and 2% (r_t=1.34 and 5.36). Even for a relatively low Görtler number, the nonlinear interactions are very strong and their influence becomes evident at short distances from the leading edge. For similar turbulence levels the nonlinear effects on the Klebanoff modes over a flat plate are very weak (refer to figure 2a of Ricco et al. [40]). Furthermore, at these

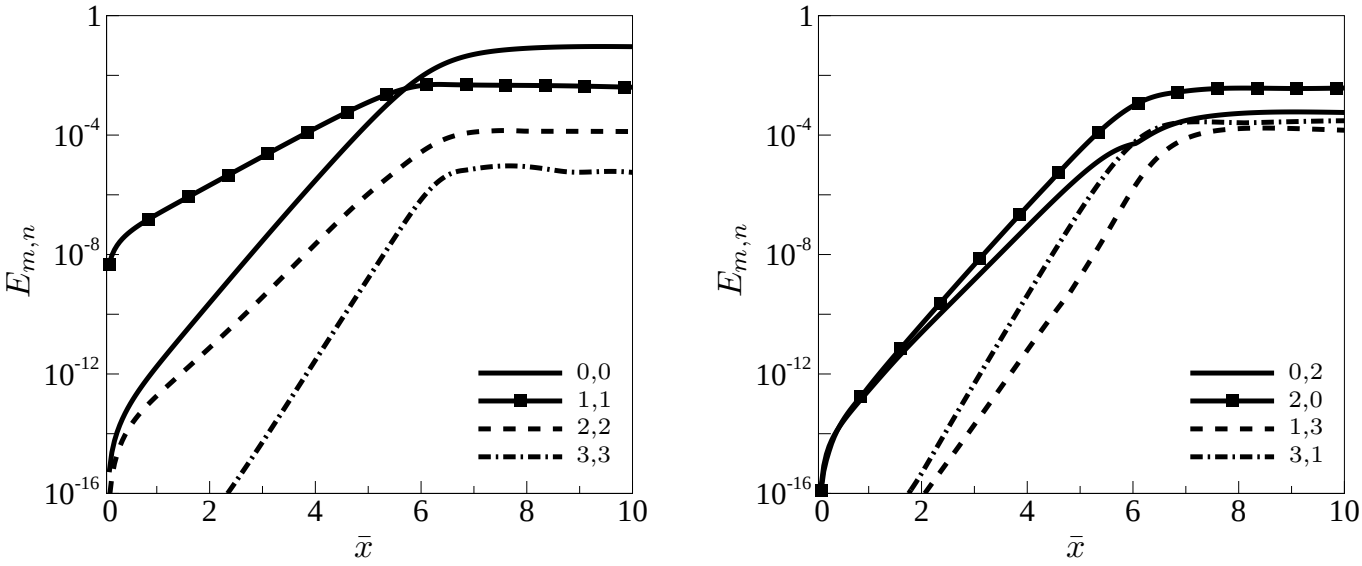

FIG. 4. Downstream development of maximum energy associated with the forced mode and nonlinearly generated harmonics at r_t=0.01 for $\mathcal{G}$=14.7 and k_x=0.00435 (refer to case 1 in table I).

elevated turbulence intensities, the Görtler vortices do not exhibit a quasi-exponential growth because nonlinearity saturates them rapidly.

The downstream evolution of $\eta_{rms,max}$ is shown in figure 3 (right). Differently from the low-r_t cases in figure 2 (right), the wall-normal peak of $u_{rms,max}$ deviates from the linear one just downstream of the leading edge and continuously moves towards the wall as $\bar{x}$ increases. No overlapping with the linear curve is detected, even at downstream locations where the nonlinear development of $u_{rms,max}$ is indistinguishable from the linearized approximation, i.e., $\bar{x}$=0.3 for r_t=5.36. Hence, in enhanced disturbance environments, the nonlinear effects are revealed first as a wallward shift of the maximum disturbance and, further downstream, as saturation of the boundary-layer fluctuations.

Figure 4 shows the downstream amplification of the maximum energy associated with each mode, i.e.,

$$E_{m,n}(\bar{x}) = r_t \max_{\eta} |\hat{u}_{m,n}(\bar{x},\eta)|^2, \tag{16}$$

for the case with r_t=0.01. Only the streamwise component of the disturbance velocity is included in (16) as it is much larger than the wall-normal and spanwise components. The forced mode (1,1) is dominant for $\bar{x}$<5, but all the other harmonics amplify more rapidly than the forced mode. Further downstream, the mean-flow distortion, i.e., the mode (0,0), becomes one order of magnitude more intense than the mode (1,1) and the second unsteady harmonic (2,0) becomes comparable with the forced mode. The other harmonics instead remain of smaller amplitude. The energy of the steady mode (0,2), shown in figure 4 (right), is about one order of magnitude lower than that of the forced mode (1,1) and the nonlinearly-generated mode (2,0). The mode (0,2) is the most intense steady spanwise-modulated disturbance produced by nonlinearity and it can reach amplitudes comparable with or even larger than the forced mode for higher r_t, therefore rendering the vortices almost steady, as shown by Dongdong et al. [15]. At $\bar{x}\approx$6, the disturbance energy saturates. For steady vortices, Hall [22] argues that the interaction between the mean-flow distortion and the forced modes determines the overall disturbance energetics. In the unsteady case, besides the energy exchange between the modes $(0,0)$ and $(1,\pm1)$, the spanwise-averaged unsteady second harmonic $(2,0)$ also gives a significant contribution to the disturbance energetics.

B. Effect of Görtler number

To investigate the influence of the Görtler number $\mathcal{G}$, two cases with different radius of curvature (case 1 and case 1r in table II) at a low turbulence Reynolds number r_t=0.01 are compared. In case 1r, r_0^* is double of that in case 1, i.e., the plate is less curved. This results in $\mathcal{G}$ being halved, while all the other parameters are constant. As shown in figure 5 (left), where $u_{rms-max}$ is displayed as a function of x/R_λ because k_x varies for the cases in the figure, increasing r_0^* attenuates the amplitude and the growth rate, and weakens the nonlinear effects. By varying the frequency of case 1, specifically by multiplying k_x by a factor $2^{2/3}$, we obtain the same Görtler number $\mathcal{G}$ employed

Case	U^*_∞ [ms^{-1}]	λ^*_z [m] $\times 10^3$	r^*_0 [m]	f^* [Hz]	R_λ	G_λ	$\hat{k}_x$	k_x $\times 10^3$	κ_z	$\mathcal{G}$	r_t
1	9.18	8	8.37	5	767	89.5	3.336	4.35	0.547	14.7	0.01
1r	9.18	8	**16.8**	5	767	44.5	3.336	4.35	0.547	7.3	0.01
1f	9.18	8	8.37	**8**	767	89.5	5.317	6.93	0.434	7.3	0.01
2	9.18	8	8.37	11	767	89.5	7.342	9.57	0.369	4.5	2.68
2r	9.18	8	*4.19*	11	767	179	7.342	9.57	0.369	9	2.68

TABLE II. Parameters for the study of the Görtler number effect. The physical parameters that are changed with respect to case 1 (case 2) are highlighted in bold (italics).

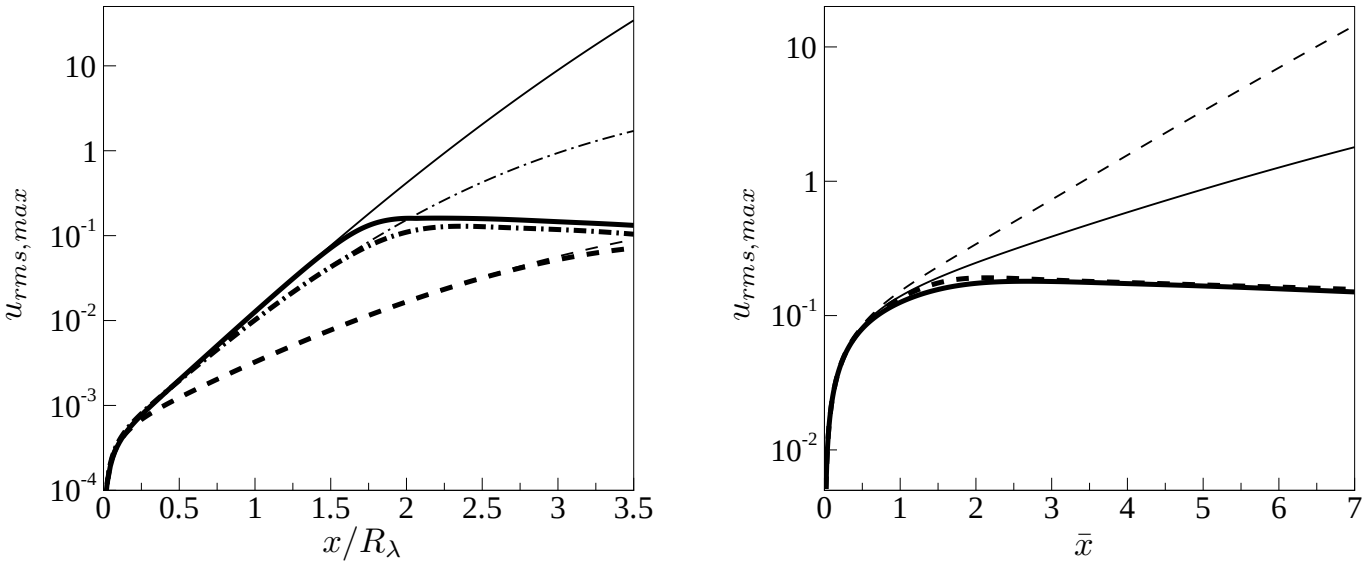

FIG. 5. Linear (thin lines) and nonlinear (thick lines) development of $u_{rms-max}$ for different Görtler numbers. Left (r_t=0.01): case 1, i.e., $\mathcal{G}$=14.7 and k_x=0.00435, (solid line), case 1r, i.e., $\mathcal{G}$=7.3 and k_x=0.00435, (dashed line), case 1f, i.e., $\mathcal{G}$=7.3 and k_x=0.00693, (dash-dotted line). Right (r_t=2.68): case 2, i.e., $\mathcal{G}$=4.5 and k_x=0.00957 (solid line), case 2r, i.e., $\mathcal{G}$=9 and k_x=0.00957 (dashed line).

in case 1r (case 1f in table II). The attenuating effect on the perturbation r.m.s. that is observed when $\mathcal{G}$ is halved is more pronounced if the reduction of $\mathcal{G}$ is due to a decreased curvature (i.e., increased r^*_0) rather than an enhanced frequency because in the latter case other effects are at play, i.e., κ_z decreases as k_x increases.

The effect of the radius of curvature is also studied in a case with relatively high free-stream turbulence intensities, i.e., r_t=2.68 (refer to case 2 and case 2r in table II). As displayed in figure 5 (right), the two nonlinear solutions for case 2 and 2r nearly coincide, while the linearized solution for case 2r is more intense than that of case 2 because of the enhanced centrifugal effects. At low $Tu(\%)$, the effect of Görtler number becomes important at streamwise locations where the disturbance undergoes a modal growth. At high $Tu(\%)$, the nonlinear response is not affected by $\mathcal{G}$ provided that the turbulence level is sufficiently intense for the nonlinear interactions to saturate rapidly and for the disturbances not to undergo an exponential growth.

C. Growth rate

As observed by Saric [43], in the case of a nonparallel base flow, the growth or decay of the boundary-layer disturbances can be calculated by tracking various quantities downstream. To measure the overall growth or decay of the vortices due to all the modes in the boundary layer, the growth rate $\bar{\alpha}$=$u'_{rms,max}(\bar{x})/u_{rms,max}$ is defined. We also introduce the definition of the growth rate and the wavenumber associated with each harmonic as the real and the imaginary parts of $\alpha_{m,n}$=$\hat{u}'_{m,n,max}(\bar{x})/\hat{u}_{m,n,max}$, where $\hat{u}_{m,n,max}$ is the maximum of $\hat{u}_{m,n}$ along η and the prime here indicates the derivative with respect to $\bar{x}$. We calculate $\alpha_{m,n}$ for (m,n)=$(\pm1,1)$, $(0,0)$, $(\pm2,0)$ because suffi-

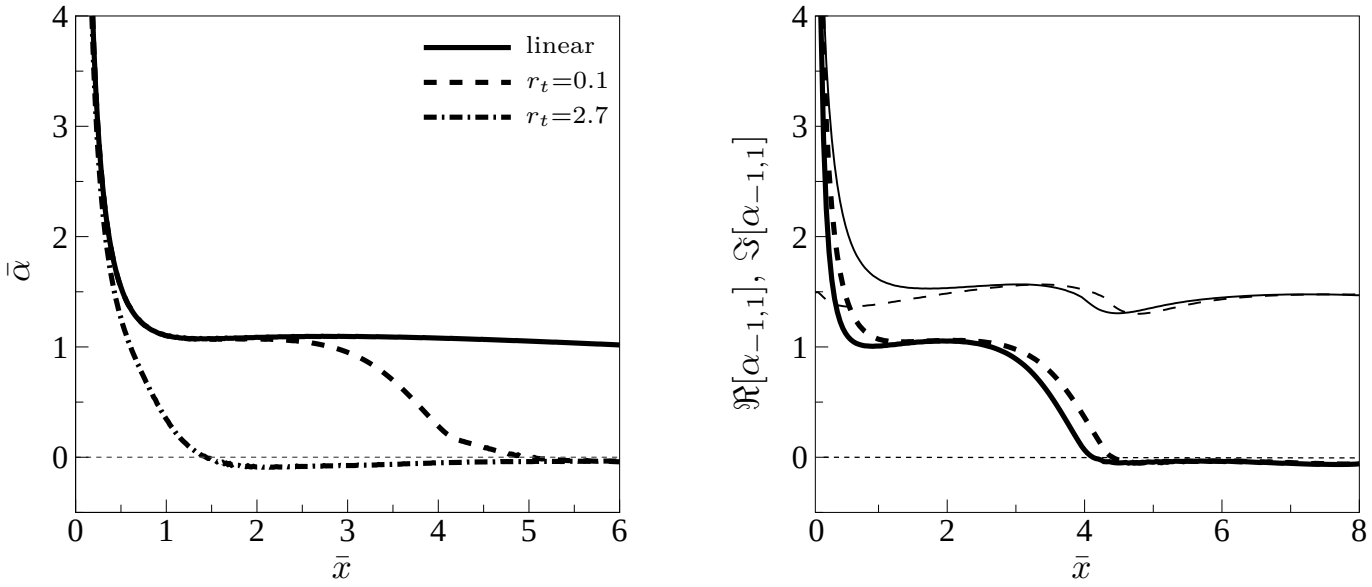

FIG. 6. Left: Local growth rate $\bar{\alpha}$ versus $\bar{x}$ for different r_t, $\mathcal{G}$=14.7 and k_x=0.00435 (refer to case 1 in table I). Right: local growth rate $\Re[\alpha_{-1,1}]$ (thick lines) and streamwise wavenumber $\Im[\alpha_{-1,1}]$ (thin lines) of the forced mode versus $\bar{x}$ for different κ_y=0.0054 (dashed line) and 5.4 (solid lines) at r_t=0.1.

ciently downstream the disturbance energetics is dominated by the forced modes, the mean-flow distortion and the spanwise-averaged second harmonic (refer to figure 4). Unless otherwise stated, the results reported in the following correspond to case 1 of table I.

Figure 6 (left) displays the local growth rate $\bar{\alpha}$ for r_t=0 (linear), 0.1 (low free-stream turbulence intensity) and 2.7 (high free-stream turbulence intensity). In the linear case, the growth rate becomes nearly independent of $\bar{x}$ for $\bar{x}$>1, thus confirming the conclusion of Wu et al. [57] that the amplification of the induced disturbance is (quasi-) exponential. For a low turbulence level, i.e., r_t=0.1, the perturbation first exhibits an exponential growth at the same rate as the linear solution. When the nonlinear interactions intensify, the growth rate decreases rapidly and tends to zero as saturation is reached. For a high turbulence level, i.e., r_t=2.7, the perturbation does not undergo modal growth. The growth rate is slightly negative for 1.5<$\bar{x}$<5 and almost null for $\bar{x}$>5 as the disturbance saturates.

In the linear study of Wu et al. [57] the wall-normal wavenumber k_y was shown to have a small effect proving the modal nature of the solution for sufficiently large Görtler numbers. We herein investigate the influence of κ_y on the growth rate and wavenumber of the nonlinearly excited perturbation for r_t=0.1. We vary κ_y from the value corresponding to case 1 in table I (κ_y=0.54) by only varying k_y, while k_x and k_z are unchanged so that κ_z remains constant. As at the beginning of §III, we set $\hat{u}^{\infty}_{x,\pm}$=1 because our definition of turbulence intensity is based on the free-stream streamwise velocity component. The normalized amplitudes of $\hat{u}^{\infty}_{y,\pm}$ and $\hat{u}^{\infty}_{z,\pm}$ are obtained from the continuity equation (1) and the constraint of constant amplitude of the free-stream velocity field, i.e., $\sqrt{(\hat{u}^{\infty}_{x,\pm})^2+(\hat{u}^{\infty}_{y,\pm})^2+(\hat{u}^{\infty}_{z,\pm})^2}=\sqrt{3}$. As shown in figure 6 (right), κ_y has to increase by three orders of magnitude to show an effect on the local growth rate $\Re[\alpha_{-1,1}]$ and wavenumber $\Im[\alpha_{-1,1}]$ of the forced mode. The influence of κ_y is most evident on $\Im[\alpha_{-1,1}]$ near the leading edge. In the regions of quasi-exponential growth (1.5<$\bar{x}$<3) and of nonlinear saturation ($\bar{x}$>5), $\Re[\alpha_{-1,1}]$ is not influenced by κ_y. Similar conclusions are drawn for $\alpha_{0,0}$ and $\Re[\alpha_{2,0}]$ and the interested reader is referred to figure 3.8 of Marensi [32].

The effect of κ_y is most intense near the leading edge and very mild when the Görtler vortices are exponentially growing or saturated because κ_y does not appear in the boundary region equations, but only in the outer boundary conditions (12) and in the initial conditions given by equations (2.43)-(2.45) in Ricco et al. [40].The boundary and initial conditions exert their influence primarily during the initial stages of the disturbance evolution where the inviscid unbalance between the centrifugal effects and the wall-normal pressure gradient has not ensued yet, while they are much less influential during the stages of modal growth and saturation of the Görtler vortices.

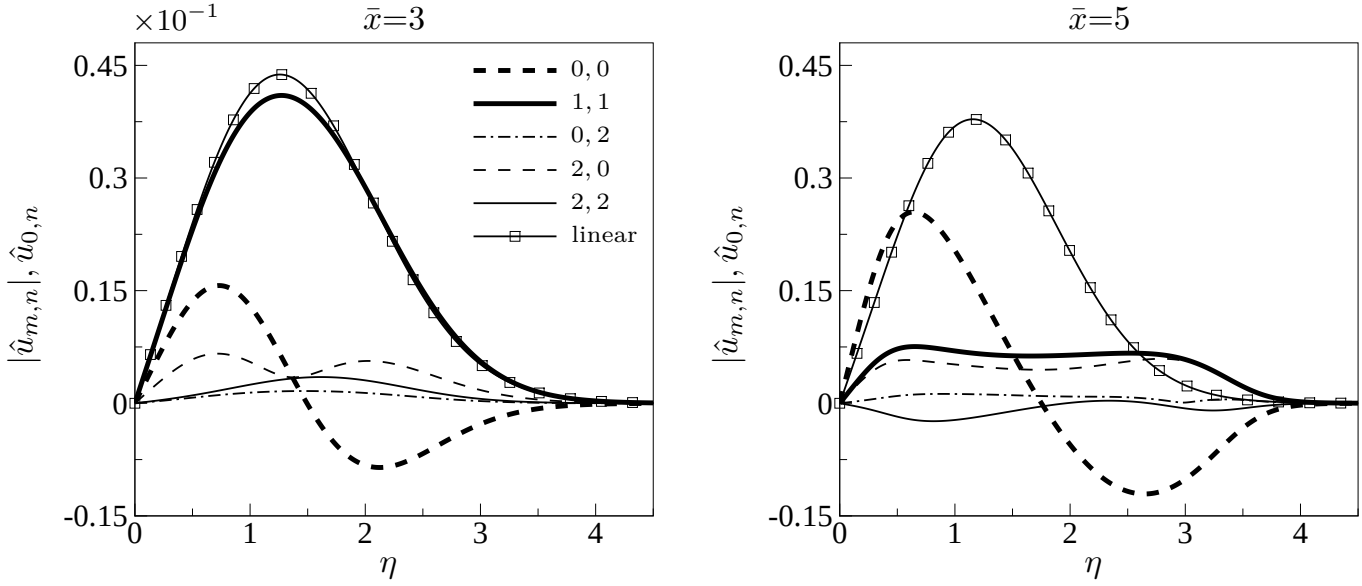

FIG. 7. Streamwise-velocity profiles of the forced mode, mean-flow distortion and second harmonics at $\bar{x}$=3 (left) and $\bar{x}$=5 (right).

D. Wall-normal profiles

The wall-normal velocity profiles for case 1 of table I are studied because this case is characterized by significant centrifugal effects. The turbulent Reynolds number is assumed to be r_t=0.1 to allow sufficient linear growth in the initial stage. The streamwise-velocity profiles of the forced mode and of the higher harmonics are shown in figures 7 at $\bar{x}$=3 and $\bar{x}$=5 (the y-axis scale in the right graph ($\bar{x}$=5) is ten times larger than in the left graph ($\bar{x}$=3)). The mode $(0,0)$, which represents the distortion of the mean flow, displays more than an order of magnitude growth from $\bar{x}$=3 and $\bar{x}$=5 and becomes larger than the forced mode $(1,1)$. The second harmonics grow significantly, in particular the spanwise-averaged harmonic (2,0), which becomes comparable with the forced mode at $\bar{x}$=5. At $\bar{x}$=3 the nonlinear profile of $r_t|\hat{u}_{1,1}|$ and its linear counterpart are similar, with a peak at η=1.3. At $\bar{x}$=5 the linear profile has retained its shape and increased in magnitude by nearly ten times. The nonlinear profile of $r_t|\hat{u}_{1,1}|$ has instead amplified less than its linearized approximation. Its shape has changed considerably as two maxima appear: the first peak is found at η=0.7 and is slightly larger, whereas the second peak is located closer to the free stream at η=3. For η>2.5, the nonlinear profile of $r_t|\hat{u}_{1,1}|$ is larger than the linear one. This nonlinear amplifying effect in the boundary-layer outer edge was also pointed out by Ricco et al. [40] for the flat-plate case, but it becomes more intense when centrifugal forces are at work. The appearance of an outer-flow peak in the $r_t|\hat{u}_{1,1}|$ profile was not observed in the flat-plate case of Ricco et al. [40].

Figure 8 (left) shows the profiles of $r_t|\hat{u}_{1,1}|$ at four $\bar{x}$ locations. At $\bar{x}$=3, the peak appearing in the core of the boundary layer moves wallward as the flow evolves downstream, while the less pronounced outer peak shifts upward. As a result, the nonlinear perturbation persist further away from the wall as compared to the linear case. The profiles displayed in figures 7 and 8 qualitatively agree with the results of Hall [22]. The near-wall peak of the mean-flow distortion, $r_t\hat{u}_{0,0}$, shown in figure 8 (right), shifts slightly closer to the wall, while the negative peak moves towards the free stream where backward jets exist [56].

The vertical and spanwise velocity profiles are shown in figure 9. As demonstrated by the scaling of the boundary-region approach (refer to §II A), the cross-flow velocity components are weaker than the streamwise velocity. The higher harmonics and the distortion of the mean flow grow by almost one order of magnitude from $\bar{x}$=3 to $\bar{x}$=5, whereas the forced mode does not amplify as much as the linear counterpart. At $\bar{x}$=5 nonlinearity attenuates the intensity of the forced mode and moves the peak towards the boundary-layer outer edge, therefore slightly strengthening the fluctuations there. The stabilizing effect of nonlinearity on the wall-normal and spanwise velocity profiles differs from the nonlinear steady results of Hall [22], who reported enhanced nonlinear profiles of the forced mode as compared to the linear ones (refer to figure 3(e,f) of Hall [22]). Analogous to the steady case [21], the trend of the linear velocity components changes only slightly with increasing $\bar{x}$, while the nonlinear forced-mode profile is modified significantly. This distortion is more intense for the streamwise velocity than for the cross-flow velocities. The wall-normal and spanwise velocities are no longer affected by the free-stream forcing at $\bar{x}$=5, implying that the disturbance has evolved

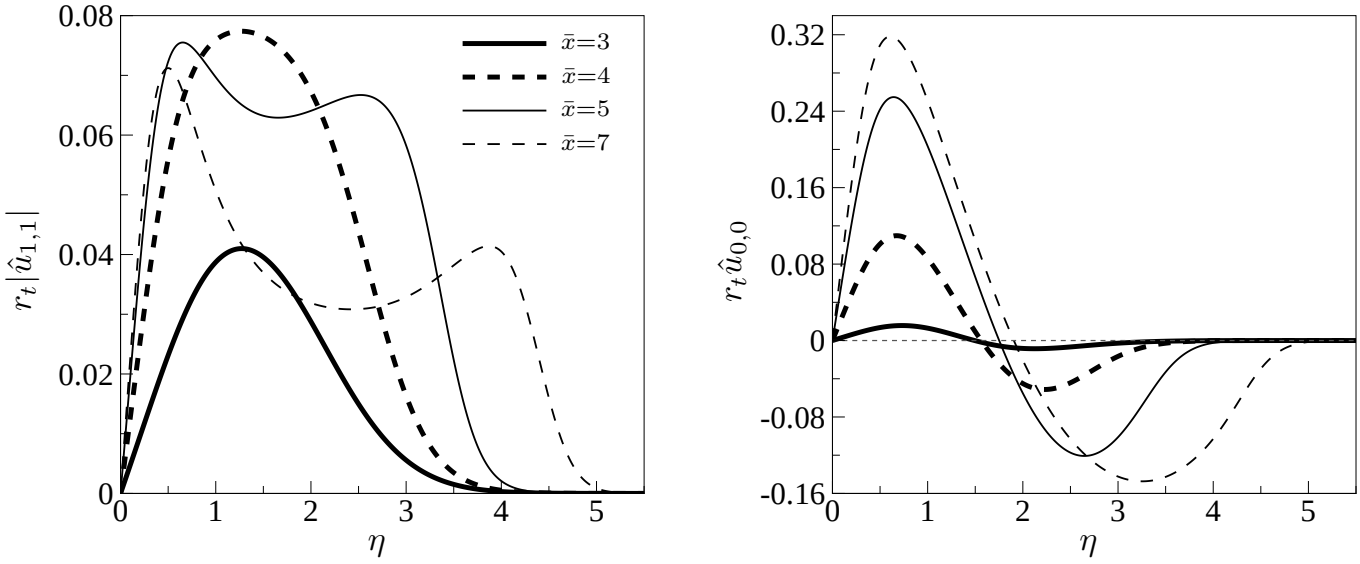

FIG. 8. Profiles of $r_t|\hat{u}_{1,1}|$ (left) and $r_t\hat{u}_{0,0}$ (right) at different $\bar{x}$.

into an eigenmode [57].

E. Comparison with experimental and DNS data

Our results are compared with experimental data and with one set of direct numerical simulations. The experimental conditions and the DNS parameters are given in table III.

	U^*_∞ [ms^{-1}]	r^*_0 [m]	λ^*_z [m]	f^* [Hz]	λ^*_x [m]	F_b	R_λ	k_x	κ_z	$\mathcal{G}$	r_t
TWS	2.85	1	0.012	1	2.85	11.6	362	0.0042	0.809	133	0.58
FB	7.5	4	0.017	5	1.5	8.4	1344	0.0113	0.256	20.6	0.19
SB	5	3.2	0.023	1	5	3.7	1257	0.0046	0.415	130	0.63
PB	2	0.65	0.03	0.5	4	13.6	549	0.0075	0.49	265	1.36
SBZ	2.85	1	0.015	4	0.7	48	450	0.0216	0.321	15.8	0.16

TABLE III. Parameters from the experiments of Tandiono et al. [52] (TWS), Finnis and Brown [16] (FB), Swearingen and Blackwelder [51] (SB), Peerhossaini and Bahri [35] (PB) and from DNS of Schrader et al. [46] (SBZ).

1. Comparison with experimental data by Tandiono et al. [52]

The experimental data by Tandiono et al. [52] are first studied. In these experiments, a series of vertical wires are positioned between the turbulence-generating screens and the leading edge of the plate in order to preset the wavelength of the Görtler vortices. The comparison is performed with their case 1, i.e., U^*_∞=2.85 m/s and λ^*_z=12 mm. Tandiono et al. [52] do not provide the frequency spectra in the pre-transitional area because the boundary-layer fluctuations are found to be quasi-steady. Time-averaging of the velocity profile is carried out in order to cut wind-tunnel noise (T. Tandiono, 2016, personal communication). In their DNS of roughness-excited Görtler rolls, Schrader et al. [46] found the growth rate of the low-frequency ($F_b\leq$16) and steady Görtler modes to be almost the same. Therefore, in our comparison with Tandiono et al. [52]'s experiments, we employ a sufficiently low frequency f^*=1 Hz (F_b=11.6) to assume the vortices to be quasi-steady. The turbulence level is Tu=0.45%.

The predicted profiles of the total streamwise velocity at the upwash ($z=\pi$) and downwash (z=0) positions at t=0 are shown in figure 10 at four streamwise locations. The Blasius solution is also displayed. We obtain good agreement for the upwash and downwash profiles inside the boundary layer up to $\tilde{\eta}=y^*\sqrt{U^*_\infty/(x^*\nu^*)}\approx$7, with our

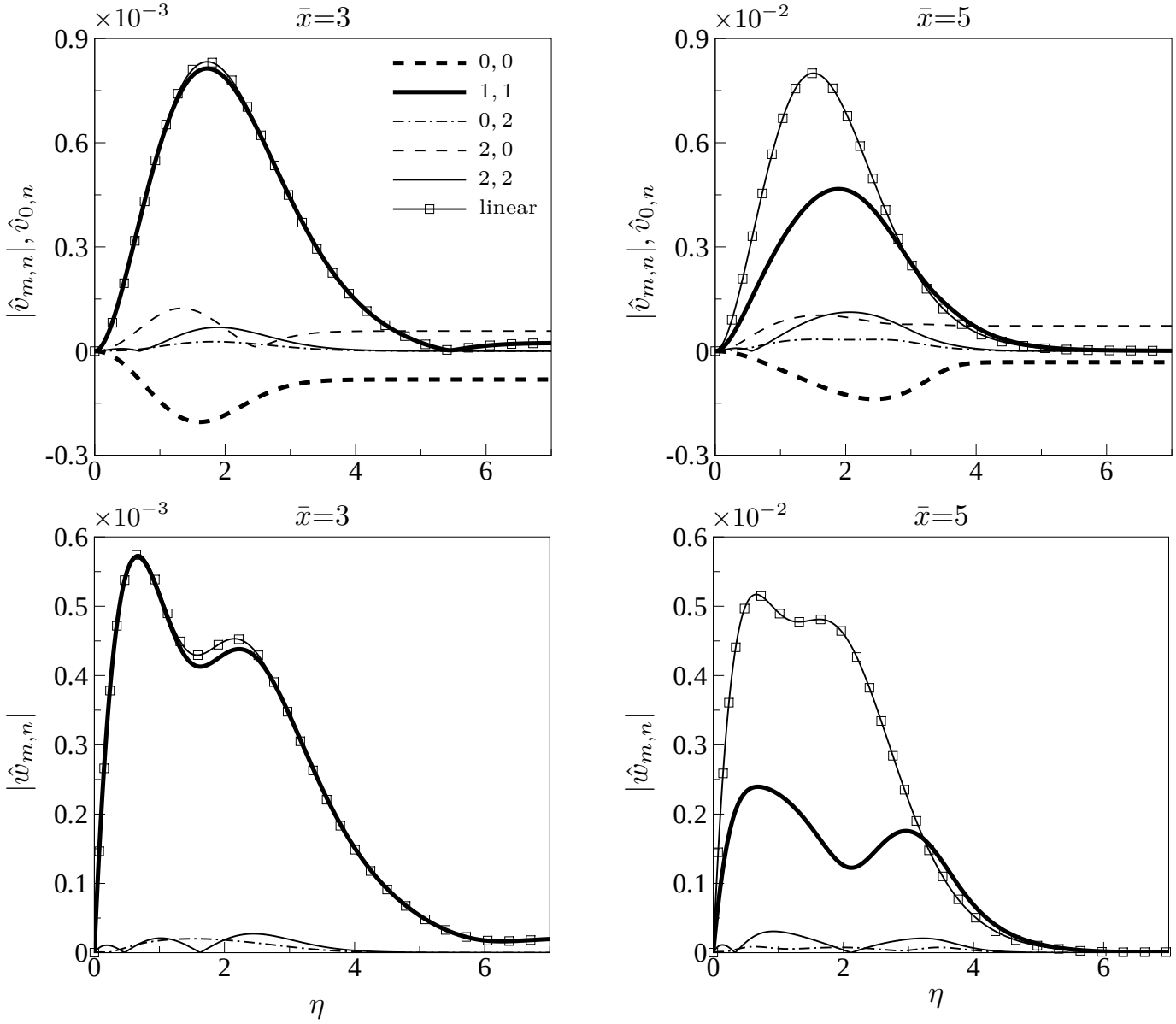

FIG. 9. Wall-normal (first row) and spanwise (second row) velocity profiles of the forced mode and higher harmonics at $\bar{x}$=3 (left) and $\bar{x}$=5 (right).

numerical simulations accurately capturing the distortion of the upwash profile. The profiles of Tandiono et al. [52] are normalized with the local free-stream streamwise velocity which is different from the mean streamwise velocity due to a slight streamwise pressure gradient. As a consequence, their profiles do not approach unity in the free stream. This explains the slight discrepancy between our results and the experimental data in the free stream. The mushroom-like structures of the streamwise-velocity contours in the cross-flow plane are also well reproduced by our simulations, as shown in figure 11.

2. Comparison with experimental data by Finnis and Brown [16]

Wu et al. [57] performed a comparison between their numerical results and the experimental data of Finnis and Brown [16]. They obtained a good agreement where the vortices evolve linearly, but this match deteriorates downstream due to the nonlinear saturation. The comparison with Finnis and Brown [16]'s data is repeated here and improved by including the effects of nonlinearity. Finnis and Brown [16] only provide an upper limit of the free-stream turbulence level in their experiments, i.e., Tu<0.15%. In our simulation Tu=0.04% is chosen to match the

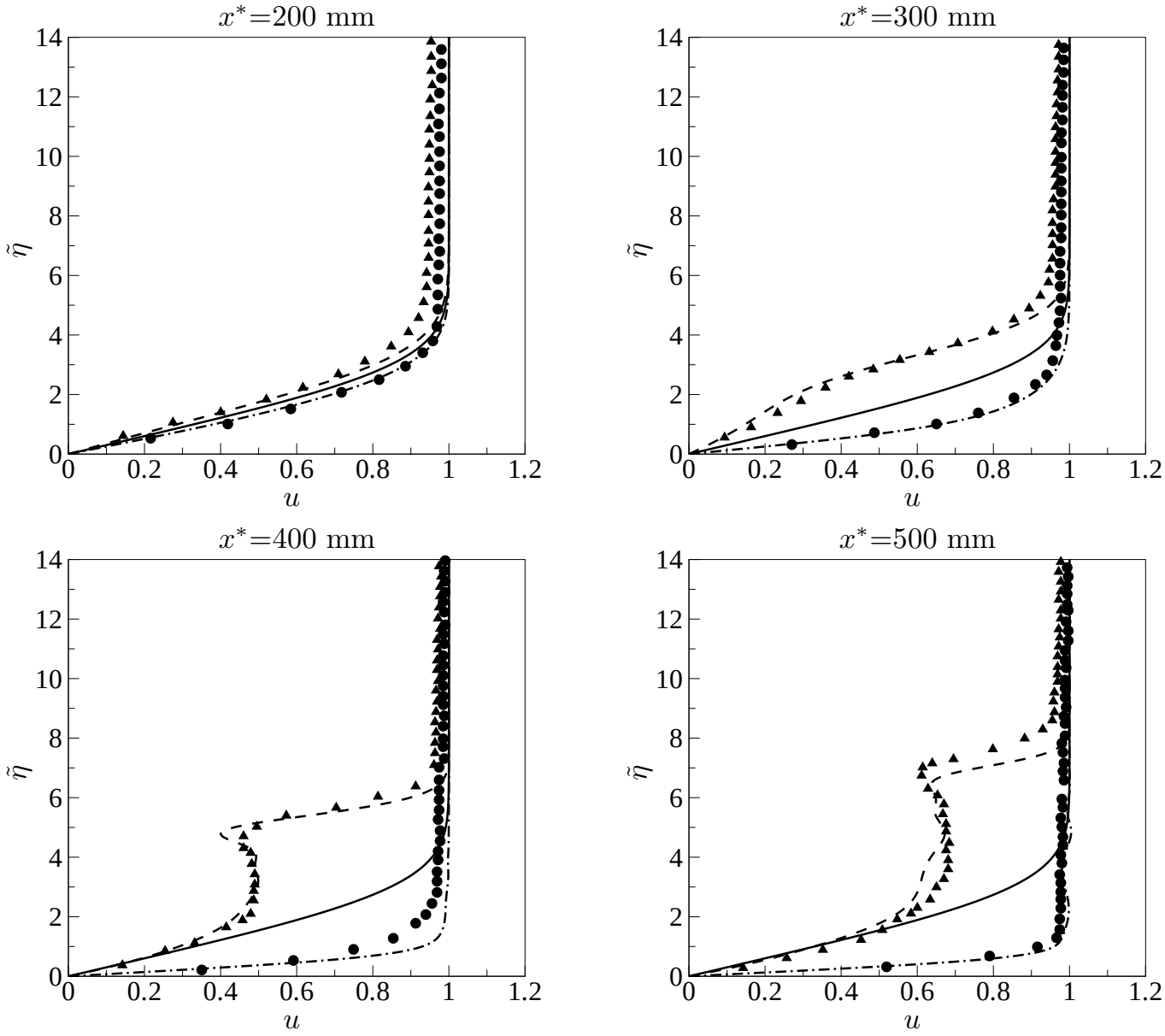

FIG. 10. Comparison between the streamwise-velocity profiles from figure 4 of Tandiono et al. [52] (symbols) and our numerical solutions (lines): Blasius (solid line), upwash (dashed line and triangles), downwash (dash-dotted line and circles). The wall-normal coordinate is $\tilde{\eta}=y^*\sqrt{U^*_\infty/(x^*\nu^*)}$, as in Tandiono et al. [52].

experiments at the first location. As shown in figure 12 (left), good agreement is obtained in the linear and nonlinear stages of the disturbance development, with the deviation due to nonlinearity being predicted by our numerical results.

3. Comparison with experimental data by Swearingen and Blackwelder [51]

The experiments of Swearingen and Blackwelder [51] focused on the development of naturally occurring Görtler vortices in the boundary layer over a concave plate with a radius of curvature r^*_0=3.2 m and free-stream velocity U^*_∞=5 m/s. A honeycomb and four fine-mesh screens were placed ahead of the test section to control the free-stream turbulence level. The measured turbulence intensity was Tu=0.07% and spanwise deviations in the free-stream velocity of less than 0.5% were detected. A turbulence intensity Tu=0.14% was used in our numerical simulation in order to best fit the experimental data at the first two streamwise locations. This is justified by the lack of more detailed

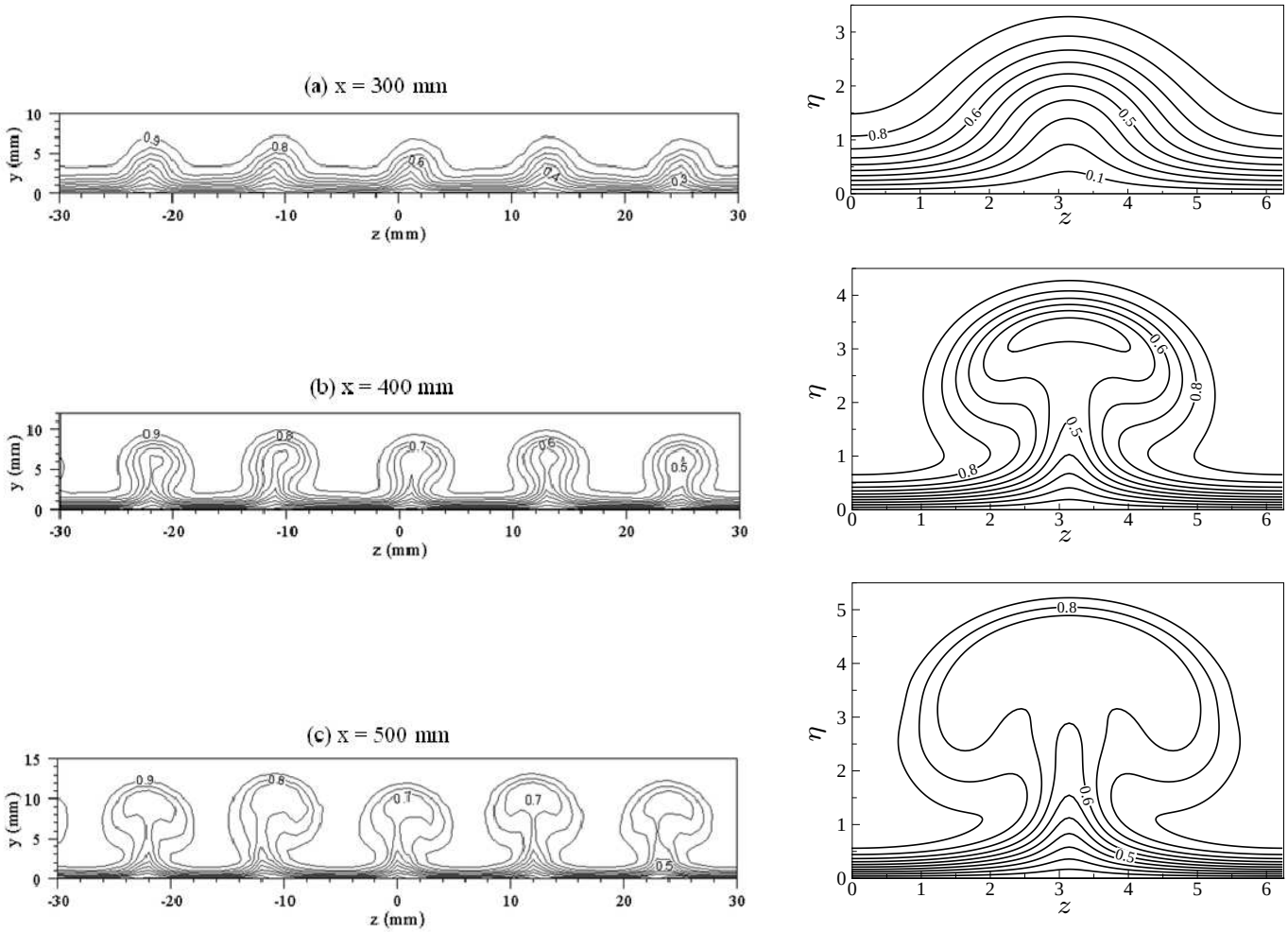

FIG. 11. Iso-contours of the streamwise velocity in the cross-flow plane at three streamwise locations. Left: measurements of Tandiono et al. [52] (adapted from their figure 2, reproduced from Tandiono, T., Winoto, S., Shah, D., 2008. On the linear and nonlinear development of Görtler vortices. Phys. Fluids 20 (9), 094103., with the permission of AIP Publishing). Right: present results.

information on the composition of the free-stream turbulence. The average spanwise wavelength and the kinematic viscosity extracted from the experiments are λ_z^*=23 mm and ν^*=1.455×10^{-5}m^2/s, respectively. The comparison between our numerical results and the experiments of Swearingen and Blackwelder [51] is shown in figure 12 (right) in terms of the streamwise evolution of $u_{rms-max}$. The linear growth rate, the location of the nonlinear saturation, and the amplitude of the saturated vortices are captured accurately by our simulations. The agreement is very good up to x^*=1 m. At the last two locations, high-frequency fluctuations due to secondary instability may have become sufficiently intense to affect the evolution of the Görtler vortices.

4. Comparison with experimental data by Peerhossaini and Bahri [35]

Peerhossaini and Bahri [35] studied the nonlinear instability of Görtler vortices triggered by free-stream grid turbulence. Measurements were taken over a concave wall with a radius of curvature r_0^*=0.65 m and with a free-stream turbulence level Tu=0.7%. The spanwise wavelength λ_z^* is approximately 30 mm. A frequency f^*=0.5 Hz was chosen for our simulations. The frequency parameter F_b=13.6 is in the range for which Schrader et al. [46] showed the growth rates of the low-frequency and unsteady Görtler vortices to be almost identical. As a check, we repeated the simulations for f^*=0.25 Hz and very similar results to those with f^*=0.5 Hz were obtained. The integral of the perturbation energy, i.e., E_u=$\int_0^\infty u'^2(y)\mathrm{d}y$, where u' represents the streamwise component of the disturbance velocity, was chosen as a measure of perturbation growth. The comparison is shown in figure 13 (left). Our numerical results

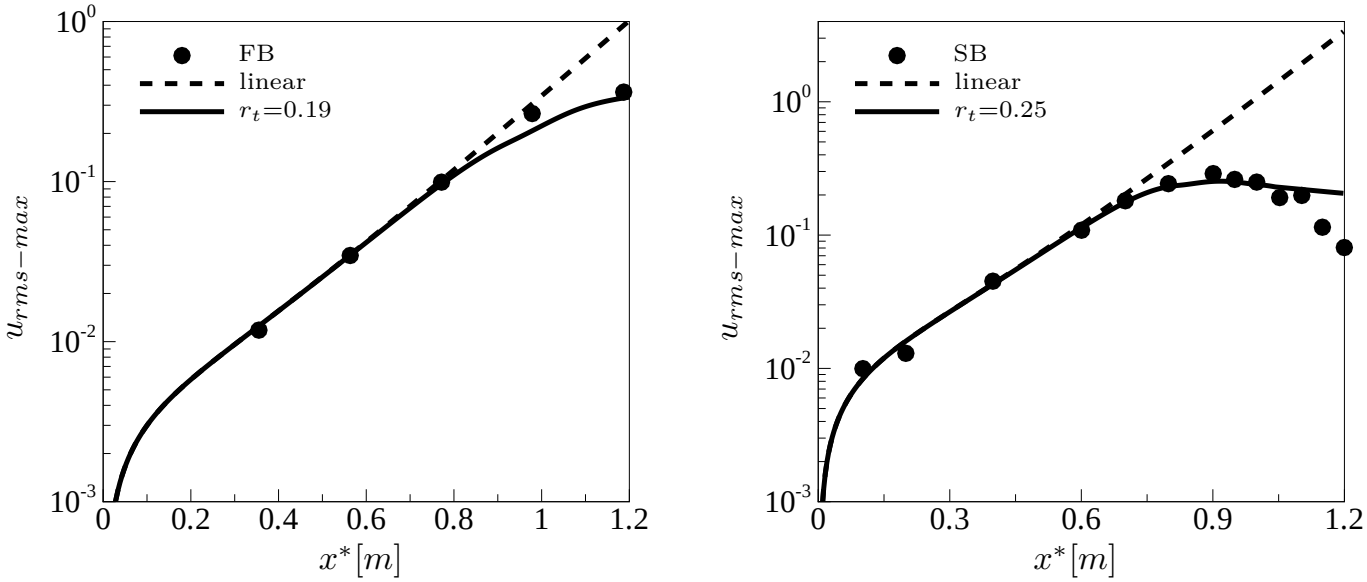

FIG. 12. Streamwise evolution of $u_{rms-max}$ and comparison with the experimental data of Finnis and Brown [16] (left) and Swearingen and Blackwelder [51] (right).

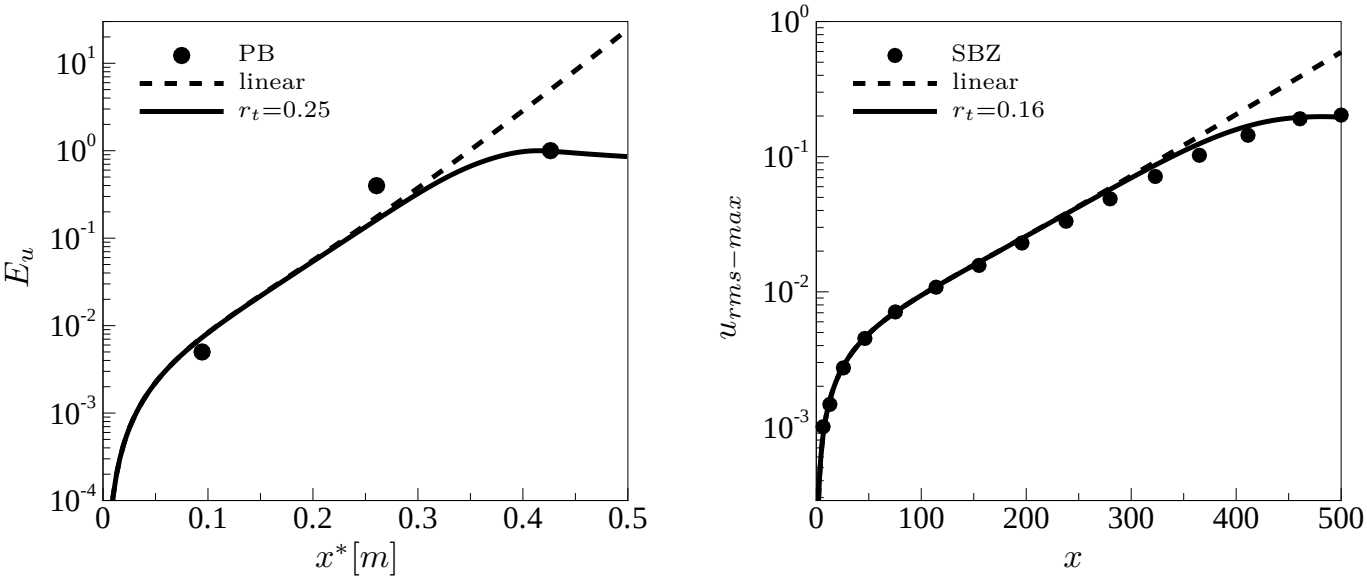

FIG. 13. Left: streamwise evolution of disturbance amplitude calculated as the integral of perturbation energy and comparison with experimental data of Peerhossaini and Bahri [35]. Right: streamwise evolution of $u_{rms-max}$ for r_t=0 and r_t=0.16 and comparison of the latter case with DNS solution from figure 22 of Schrader et al. [46].

predict the nonlinear saturation to occur at $x^*\approx$0.43 m, but the perturbation energy at x^*=0.26 m is half of the experimental value. This discrepancy can be ascribed to the uncertainty in the evaluation of λ_z^* and to the lack of information on the composition of the free-stream disturbance. The wall-normal profiles of the streamwise velocity disturbance at two locations are also compared in figure 14. The shape of the profiles agrees well with our results, with the profile at x^*=0.425 m exhibiting the two distinct peaks. At x^*=0.26 m our simulation predicts a lower peak than the experiments, resulting in a lower perturbation energy, as shown in figure 13 (left). At x^*=0.425 m the numerical peak closer to the free stream is slightly less intense than the experimental data, while the peak closer to the wall is slightly stronger. The resulting integral of the perturbation energy is very close to the experimental data, again consistently with figure 13 (left).

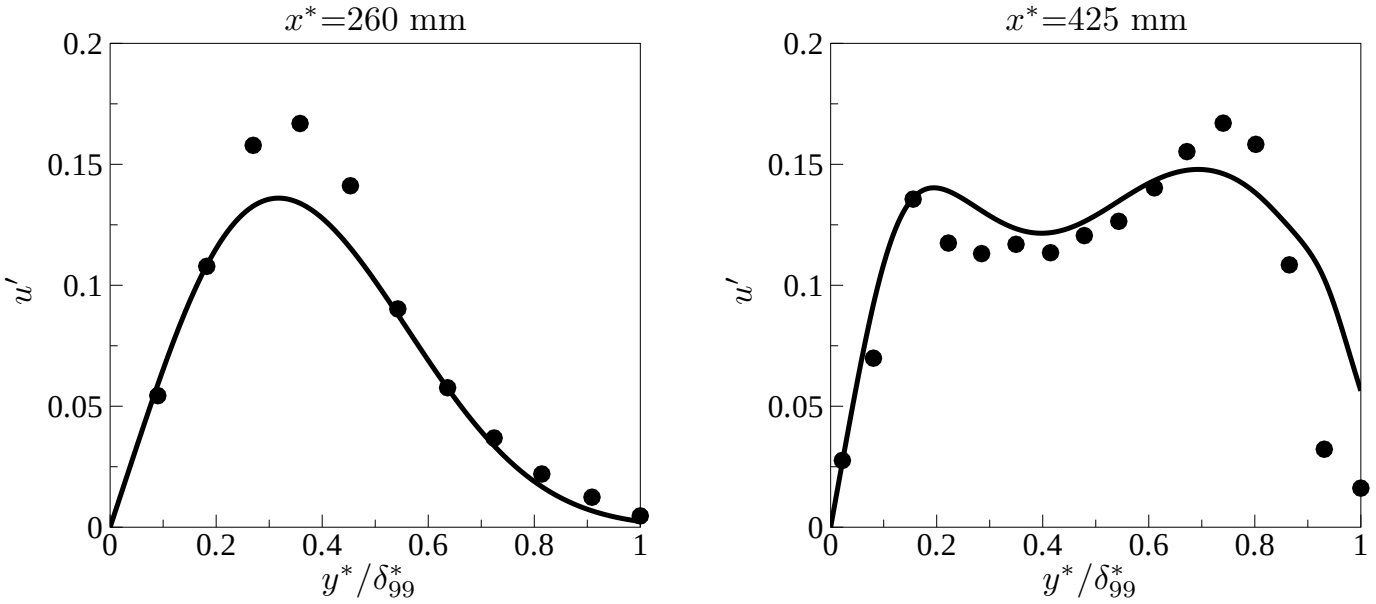

FIG. 14. Comparison between the streamwise-velocity profiles from figure 7b and 7c of Peerhossaini and Bahri [35] (symbols) and our numerical solutions (lines).

5. Comparison with direct numerical simulation data by Schrader et al. [46]

Finally, a comparison with the DNS results of Schrader et al. [46] is performed. Schrader et al. [46] studied the impact of broadband free-stream turbulence with different frequency spectra and intensities on Görtler boundary layers. The free-stream turbulence field indicated as FST3 in their table 4 is selected for our comparison. This turbulence field is characterized by low-frequency components f^*=2 − 32.5 Hz and is nearly isotropic in the cross-flow plane. The turbulence level is Tu=0.1%. The frequency and the spanwise wavenumber correspond to the most energetic unsteady perturbation present in the boundary layer, according to their figure 23. In figure 13 (right) we compare the predicted streamwise velocity r.m.s with the results by Schrader et al. [46]. The linearized solution is also displayed to show that nonlinear interactions are at play. Our numerical solution matches the DNS data very well up to x=200, after which the agreement slightly deteriorates because of a lower perturbation growth rate in the DNS as compared to our solution. At this location transition starts and small-scale fluctuations affect the disturbance r.m.s., which may explain the little discrepancy observed in this region.

F. Wall transpiration

The effect of wall transpiration is studied for the flow parameters of case 1 of table I and r_t=0.1. Three factors are considered to quantify the effect of the control: the linear growth rate $\bar{\alpha}_l$, the location $\bar{x}_s$, and the saturation amplitude u_s, defined as follows. The growth rate $\bar{\alpha}_l$ is calculated by averaging $\bar{\alpha}(\bar{x})$ over the downstream region where the growth of the corresponding uncontrolled case is quasi-exponential (refer to figure 6, case r_t=0.1) because the vortices do not undergo a modal stage in the wall-transpiration case. The saturation location $\bar{x}_s$ is defined as the downstream position where $\bar{\alpha}_l(\bar{x})$ first crosses the zero and the saturation amplitude is defined as u_s=$u_{rms-max}(\bar{x}_s)$. The control is effective if $\bar{\alpha}$ and u_s are reduced and $\bar{x}_s$ is shifted downstream.

A_w	$\bar{\alpha}_l$	$\bar{x}_s$	u_s
0	1.09	4.96	0.184
-1	0.98	5.49	0.168
-2	0.85	6.74	0.139

TABLE IV. Mode (0,0).

Steady two-dimensional suction, i.e., $\hat{v}_{0,0}(\eta$=0)=A_w with A_w<0, is considered first. Figure 15 shows the downstream

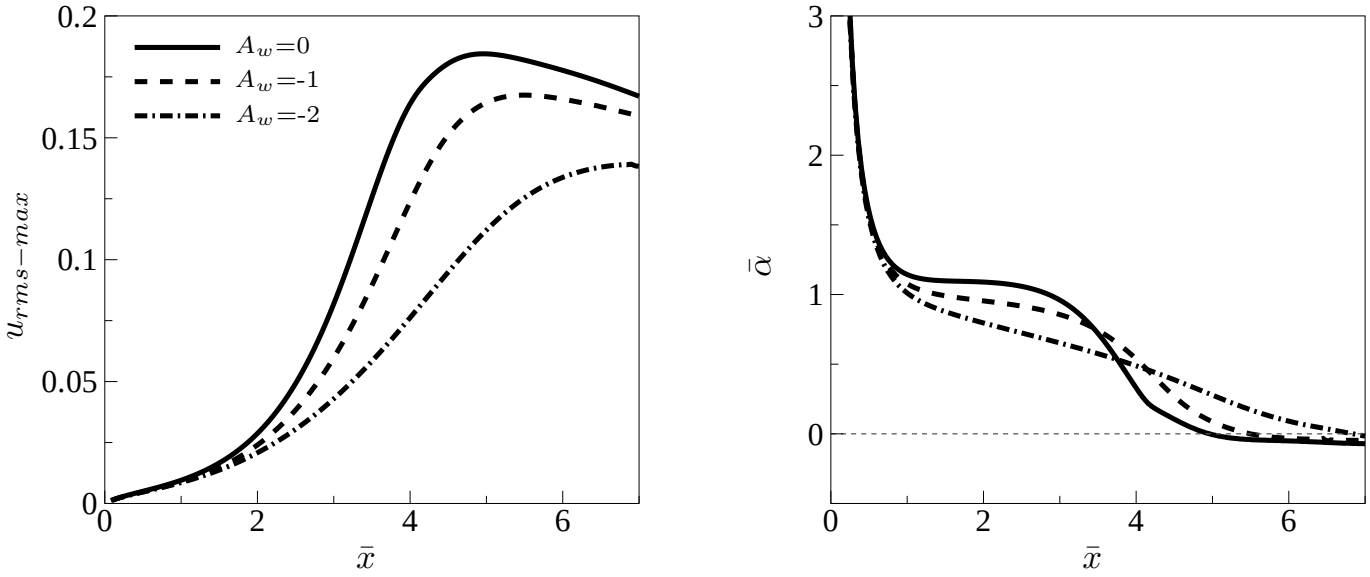

FIG. 15. Effect of A_w on the downstream evolution of $u_{rms-max}$ (left) and growth rate $\bar{\alpha}$ (right) for the case where suction is applied on the mode $(0,0)$.

development of the maximum u_{rms} and of the growth rate for different forcing amplitudes. The control of mode (0,0) is beneficial as both the intensity and the growth rate of the disturbance are attenuated. This effect is enhanced as the forcing amplitude is increased (refer also to table IV). The cases where the control is applied on the first and second spanwise harmonics, i.e., $\hat{v}_{0,n}(\eta{=}0){=}A_w$ (with n=1, 2), are shown in figures 16 and 17. The effect of wall transpiration on the modes (0,3) and (0,4) is not shown as it was found to be very weak and slightly detrimental.

The flow fields for wall-transpiration odd modes, $n = 1, 3$, are independent of the sign of A_w, while for even modes, $n = 2, 4$, the boundary-layer signature depends on the sign of A_w. It follows that the sign of A_w has an impact only when the wall-forcing is applied to those modes generated nonlinearly by the free-stream oblique modes in the uncontrolled case[32, 38]. This is because these modes have indexes $|m| + |n|$ equal to an even integer, which is the case in our control strategy for n=2,4 because we only consider steady wall transpiration, i.e., m=0.

For n=1 the effect of the control is much more marked than for n=2 as a dramatic decrease of the saturation amplitude is achieved. For n=2, wall transpiration with $A_w{<}0$ is detrimental whereas $A_w{>}0$ is slightly beneficial. As shown in table V, as $|A_w|$ is increased from 0 to 3, u_s becomes less than half that of the uncontrolled case while the saturation location moves upstream and the growth rate first slightly decreases up to $|A_w|$=1 and then slightly increases. The case $|A_w|$=2 is considered the optimal compromise among these effects because a significant reduction of u_s is obtained (almost by 60%), with a slight increase of $\bar{\alpha}_l$ (less than 5%) and a limited upstream shift of $\bar{x}_s$ (just above 30%). Increasing A_w to 3 would only bring an additional 5% decrease of u_s with the other two effects being further deteriorated (refer also to figure 16). From the scaling introduced in §II it follows that, even in the case with the strongest suction, i.e., $|A_w|$=3, the actual amplitude of the wall forcing $|v_w|{=}\sqrt{2\bar{x}k_x/R_\lambda}|A_w|$ is very small as $k_x{\ll}R_\lambda$. For example, this would correspond to $|v_w^*(\bar{x}{=}1.13)|{=}0.86\%U_\infty^*$ in the experiments of Swearingen and Blackwelder [51] and $|v_w^*(\bar{x}{=}5.02)|{=}2.76\%U_\infty^*$ in Finnis and Brown [16]. The amplitudes are calculate at the downstream location of nonlinear saturation where the effect of the control is most pronounced.

$\lvert A_w\rvert$	$\bar{\alpha}_l$	$\bar{x}_s$	u_s
0	1.09	4.96	0.184
0.5	0.866	4.33	0.147
1	1.009	3.84	0.109
2	1.144	3.32	0.080
3	1.27	2.99	0.070

TABLE V. Mode (0,1).

The wall-normal profiles of $\hat{u}_{m,n}$ for the optimal controlled case (refer to case $|A_w|$=2 in table V) are shown in figure 18. The $(0,0)$ mode is dominant in both cases and its amplitude and wall gradient are intensified by the control. Wall

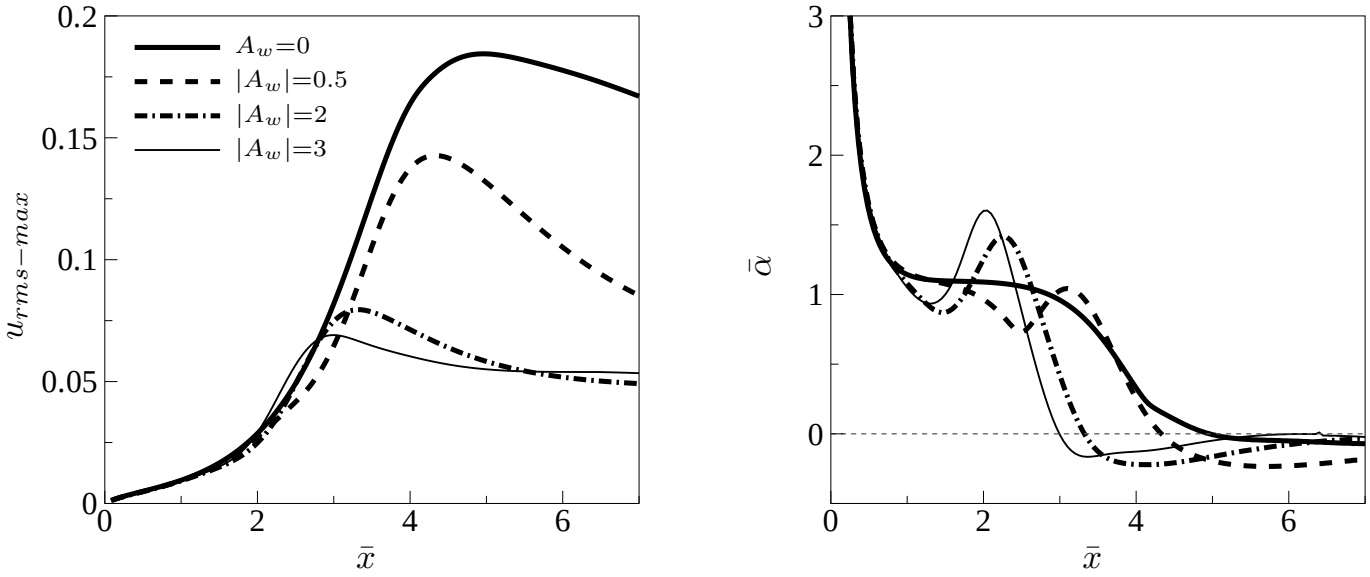

FIG. 16. Effect of A_w on the downstream evolution of $u_{rms-max}$ (left) and growth rate $\bar{\alpha}$ (right) for the case where wall transpiration is applied on the mode $(0, 1)$.

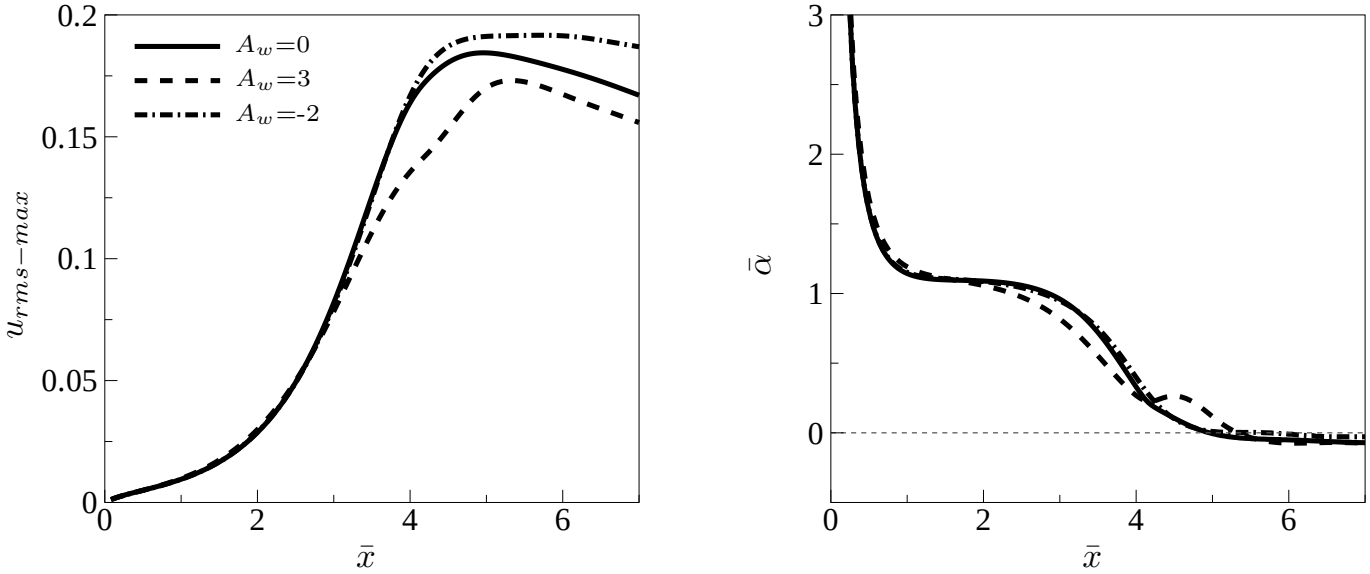

FIG. 17. Effect of A_w on the downstream evolution of $u_{rms-max}$ (left) and growth rate $\bar{\alpha}$ (right) for the case where wall transpiration is applied on the mode $(0, 2)$.

A_w	$\bar{\alpha}_l$	$\bar{x}_s$	u_s
0	1.09	4.96	0.184
1	1.071	5.11	0.176
2	1.055	5.27	0.172
3	1.057	5.34	0.173
-2	1.086	5.72	0.192

TABLE VI. Mode (0,2).

transpiration thus enhances the nonlinear growth of the wall-shear stress. As already pointed out, in the uncontrolled case the modes $(0, 1)$ and $(1, 0)$ are null. By forcing the mode $(0, 1)$ at the wall, all the harmonics arise. The magnitude

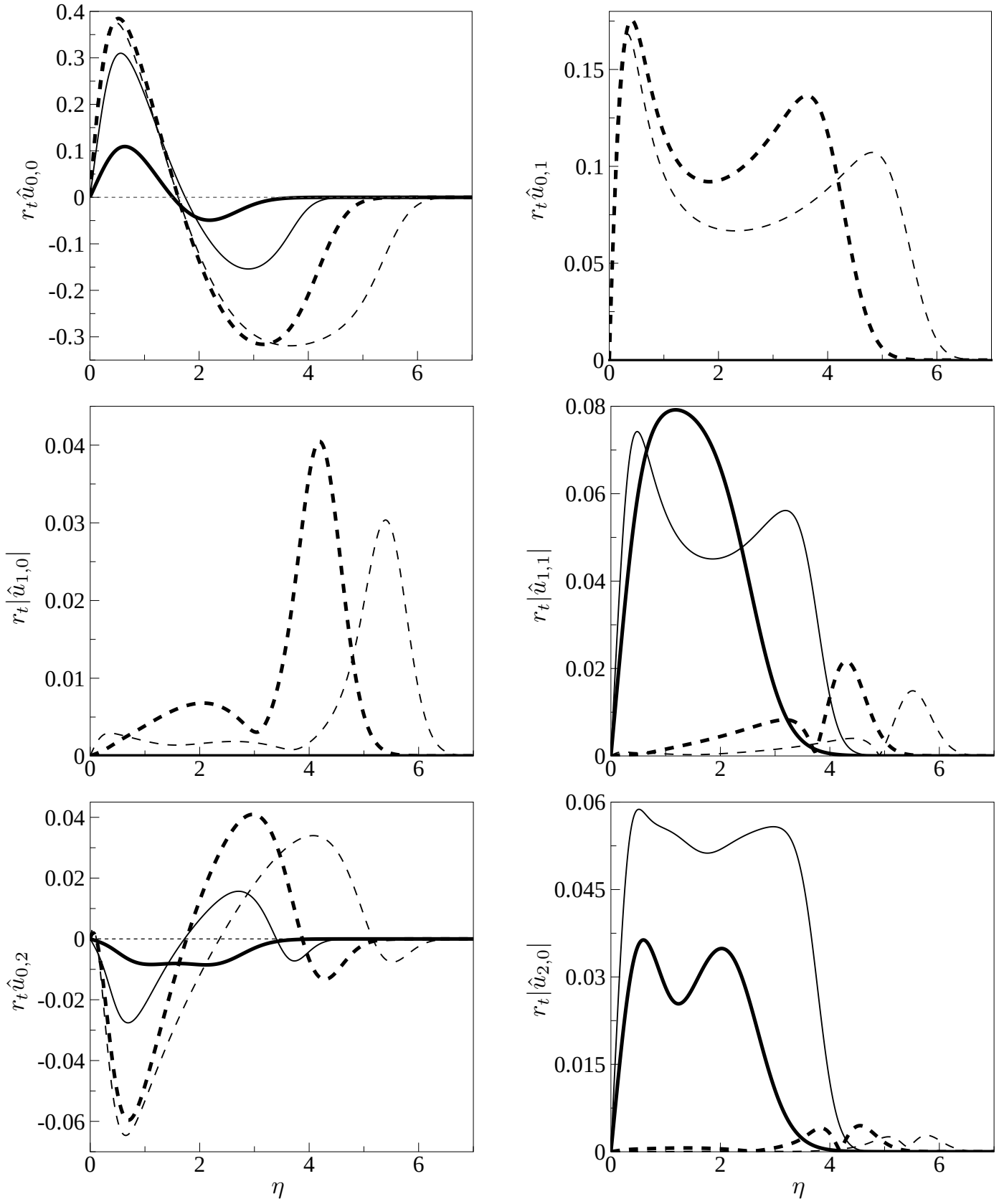

FIG. 18. Streamwise velocity profiles of the mean-flow distortion, forced mode and higher harmonics at $\bar{x}$=4 (thick line) and $\bar{x}$=6 (thin line) for the uncontrolled (solid line) and the optimal controlled (dashed line) cases. The latter correspond to the case $|A_w|$=2 in table V.

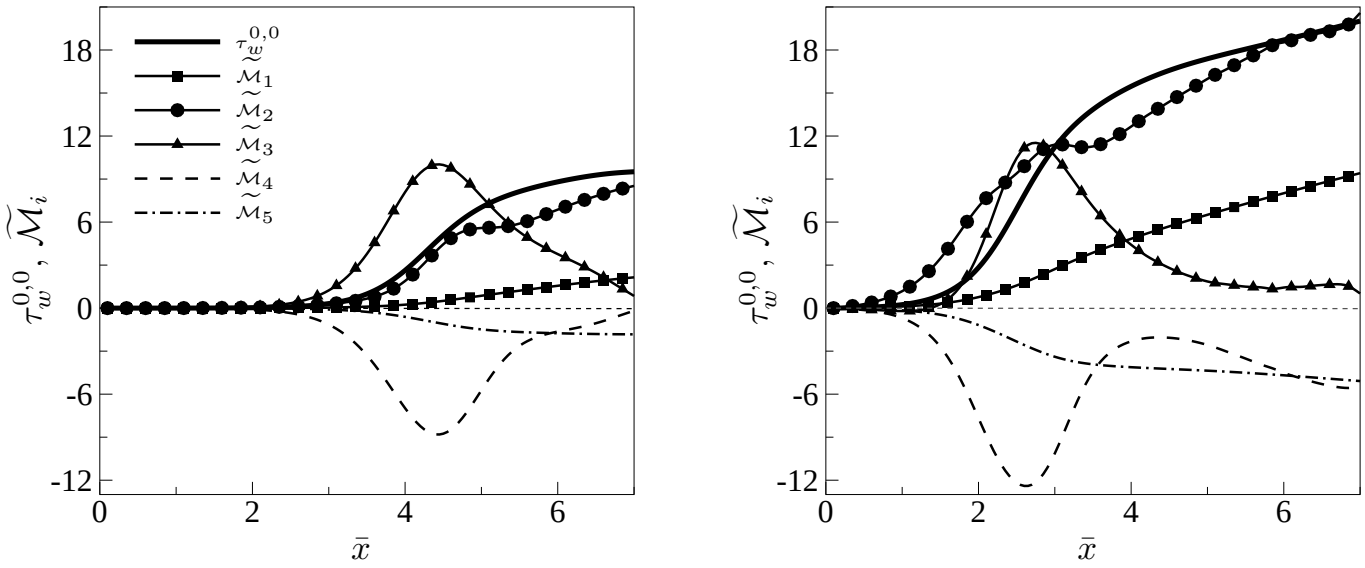

FIG. 19. Nonlinear evolution of the wall-shear stress $\tau_w^{0,0}$ and of its integral contributions $\widetilde{\mathcal{M}}_i$, as defined in the identity (15) for the uncontrolled (left) and optimally controlled (right) cases.

of $\hat{u}_{0,1}$ is comparable to that of the mean-flow distortion and almost one order of magnitude larger than the other modes. The mode $(1,0)$ has similar amplitude and shape to the forced mode. Wall transpiration strongly inhibits the forced mode (1,1) and the second harmonic (2,0). The former undergoes a considerable distortion: the wall gradient is significantly attenuated and the two peaks are shifted further from the wall, with the peak close to the free stream becoming more pronounced. The enhancing effect of the disturbance near the free stream is also observed on the other harmonics. By intensifying the nonlinear effects, especially the mean-flow distortion given by mode (0,0), the wall transpiration causes a marked stabilization of the boundary-layer disturbances and an increased nonlinear growth of the wall shear-stress as compared to the uncontrolled case.

G. Analysis of the nonlinear increase of the wall-shear stress

The increase of wall-shear stress is further studied through the integral relation (15). The downstream development of the wall-shear stress $\tau_w^{0,0}$ and of its integral contributions are shown in figure 19 (left) without wall transpiration and in figure 19 (right) with wall transpiration. In the uncontrolled case, the nonlinear effects, and thus $\tau_w^{0,0}$ and $\widetilde{\mathcal{M}}_i$, are negligible up to $\bar{x}$≈2.5. After this location, $\tau_w^{0,0}$ closely follows the convective term $\widetilde{\mathcal{M}}_2$, while $\widetilde{\mathcal{M}}_3$ and $\widetilde{\mathcal{M}}_4$ have opposite signs and balance each other.

Downstream from $\bar{x}$≈4.5, $\widetilde{\mathcal{M}}_1$ and $\widetilde{\mathcal{M}}_5$ increase slightly but almost cancel out, while $\widetilde{\mathcal{M}}_3$ and $\widetilde{\mathcal{M}}_4$ are still of very similar opposite magnitude but decay to zero as the dynamics of $\tau_w^{0,0}$ is almost entirely regulated by $\widetilde{\mathcal{M}}_2$. The balance between $\widetilde{\mathcal{M}}_3$ and $\widetilde{\mathcal{M}}_4$ denotes the almost pure interaction between the convective transport of the wall-normal velocity $\hat{v}_{0,0}$ due to the Blasius shear ($\widetilde{\mathcal{M}}_3$) and the averaged downstream rate of change of the streamwise Reynolds stresses, $\widehat{\overline{uu}}|_{0,0}$ ($\widetilde{\mathcal{M}}_4$). The integral relation (15) therefore reveals the key result that the increase of the wall-shear stress is almost only due to $\widetilde{\mathcal{M}}_2$, caused by the convective streamwise transport of $\hat{u}_{0,0}$ by the Blasius velocity F'.

All the terms $\widetilde{\mathcal{M}}_i$ on the right-hand side of (15) are intensified (in absolute value) by the control. In the presence of wall transpiration, the wall-shear stress $\tau_w^{0,0}$ starts growing much closer to the leading edge than in the uncontrolled case, i.e., from $\overline{x} = 1$, primarily because of $\widetilde{\mathcal{M}}_2$, which is the term amplified the most by the wall transpiration. While the term $\widetilde{\mathcal{M}}_3$ is largely unaffected by the control, further downstream the enhanced $\widetilde{\mathcal{M}}_1$ is now almost completely balanced by the two terms that only involve the streamwise velocity disturbance with respect to the Blasius flow, i.e., $\widetilde{\mathcal{M}}_5$ (like in the uncontrolled case) and $\widetilde{\mathcal{M}}_4$, which is not negligible when wall-transpiration occurs.

IV. SUMMARY

This paper has presented theoretical and numerical results on the generation and nonlinear development of unsteady Görtler vortices in an incompressible boundary layer over a concave wall. Görtler rolls are excited by free-stream vortical disturbances, whose amplitudes are large enough for the boundary-layer response to become nonlinear at downstream locations where the spanwise wavelength is comparable with the local boundary-layer thickness. Only the low-frequency components of the oncoming perturbation are of interest, as they are known from experiments to penetrate and amplify the most into the boundary layer. The present mathematical framework follows that of Ricco et al. [40] for the nonlinear evolution of Klebanoff modes over a flat plate and extends it to account for centrifugal effects caused by the concavity of the wall. The formation and development of the induced disturbances are governed by the nonlinear unsteady boundary-region equations, with the centrifugal force included. The influence of the upstream and free-stream forcing is taken into account by imposing the appropriate initial and far-field boundary conditions, which are shown to be the same as those employed by Ricco et al. [40].

Nonlinearity has an attenuating impact on the boundary-layer signature and this effect is significantly enhanced in the presence of a concave wall. The wall-normal profiles of the streamwise velocity undergo a pronounced shape modification as the flow evolves downstream due to a shift of the perturbations towards the outer edge of the boundary layer.

Sufficiently downstream the nonlinear solutions obtained with different values of Tu are stabilized to the same level, proving that the initial amplitude of the disturbance becomes unimportant. At low turbulence intensities the perturbation exhibits a quasi-exponential growth with the growth rate being intensified for more curved walls and longer wavelengths. At moderate turbulence levels, which are typical of turbomachinery applications, the Görtler vortices do not undergo an exponential growth because nonlinear effects come into play and saturate rapidly. As a result, for sufficiently high Tu the wall curvature, which only affects the exponentially growing part of the disturbance, does no influence the boundary-layer response. While the majority of the studies on Görtler flows have focused on steady vortices, unsteadiness is shown to have a considerable effect on the overall disturbance energetics when the boundary layer is subject to free-stream turbulence. In the unsteady case, in addition to the energy exchange between the forced mode and the mean-flow distortion, which has been observed in steady analyses, the contribution of the spanwise-averaged harmonic with double the frequency of the forced mode becomes significant.

An extensive comparison with experimental and DNS data has also been carried out and very good quantitative agreement has been obtained. We have also shown that steady spanwise modulated wall transpiration can increase the wall-shear stress, thus rending the boundary layer more stable and markedly attenuating the growth of the Görtler vortices. The enhanced wall-shear stress has been further studied by a novel integral relation involving the convective terms of the streamwise momentum equation.

Future directions include the extension of the present analysis to account for compressibility effects in high-speed boundary-layer flows. Such an investigation is of particular interest for turbomachinery applications as Görtler vortices increase the heat transfer between the pressure surfaces of gas-turbine blades and the working fluid [8]. Our theoretical approach will again provide the rigorous upstream perturbation, its entrainment into the boundary layer, and the interaction of the boundary layer with the far-field continuous forcing. Finally, the present model where the oncoming perturbation is synthesized by a pair of oblique modes will be extended to account for a continuum of free-stream low-frequency components [60], which are relevant disturbances triggering bypass transition.

ACKNOWLEDGMENTS

We would like to thank the Institute of High Performance Computing in Singapore and the University of Sheffield for funding this research. This work was supported by the A*STAR Computational Resource Centre through the use of its high performance computing facilities. Part of this material is based upon work carried out by P.R. and supported by the Air Force Office of Scientific Research under award number AFOSR Grant FA9550-15-1-0248. P.R. was also supported by UKTC EPSRC grant EP/L000261/1. The authors are also indebted to Dr Vinh-Tan Nguyen for the fruitful discussions and to Dr Daniel Wise for valuable comments on a preliminary version of the paper. We also thank Dr Tandiono Tandiono for sending us a copy of his iso-contours shown in figure 11 (left) and the Referees for the very useful comments.

Appendix: Derivation of the integral relation for the wall-shear stress

Equation (15) is derived as follows. The streamwise momentum equation (7) is first integrated from 0 to η. The wall-normal gradient of the mode $\hat{u}_{0,0}$ at the wall is then isolated on the left-hand side (l.h.s.):

$$\left.\frac{\partial \hat{u}_{0,0}}{\partial \eta}\right|_{\eta=0} = \frac{\partial \hat{u}_{0,0}}{\partial \eta} - 2\bar{x}r_t\widehat{\bar{u}\bar{v}}_{0,0} + \int_0^\eta \eta F''\hat{u}_{0,0}\mathrm{d}\eta - 2\bar{x}\int_0^\eta F'\frac{\partial \widehat{u}_{0,0}}{\partial \bar{x}}\mathrm{d}\eta + \int_0^\eta F\frac{\partial \widehat{u}_{0,0}}{\partial \eta}\mathrm{d}\eta \tag{A.1}$$
$$- 2\bar{x}\int_0^\eta F''\hat{v}_{0,0}\mathrm{d}\eta - 2r_t\bar{x}\int_0^\eta \left.\frac{\partial \widehat{\bar{u}\bar{u}}}{\partial \bar{x}}\right|_{0,0}\mathrm{d}\eta + r_t\int_0^\eta \eta\left.\frac{\partial \widehat{\bar{u}\bar{u}}}{\partial \eta}\right|_{0,0}\mathrm{d}\eta.$$

Further integration between 0 and η leads to:

$$\eta\left.\frac{\partial \hat{u}_{0,0}}{\partial \eta}\right|_{\eta=0} = \hat{u}_{0,0} - 2\bar{x}r_t\int_0^\eta \widehat{\bar{u}\bar{v}}|_{0,0}\mathrm{d}\eta + \int_0^\eta\int_0^\eta \mathcal{I}(\bar{x},\eta)\mathrm{d}\eta\mathrm{d}\eta, \tag{A.2}$$

where

$$\mathcal{I}(\bar{x},\eta) = \eta F''\hat{u}_{0,0} - 2\bar{x}F'\frac{\partial \hat{u}_{0,0}}{\partial \bar{x}} + F\frac{\partial \hat{u}_{0,0}}{\partial \eta} - 2\bar{x}F''\hat{v}_{0,0} - 2r_t\bar{x}\left.\frac{\partial \widehat{\bar{u}\bar{u}}}{\partial \bar{x}}\right|_{0,0} + r_t\eta\left.\frac{\partial \widehat{\bar{u}\bar{u}}}{\partial \eta}\right|_{0,0}.$$

The no-slip condition on the streamwise velocity has been used for both integrations. Equation (A.2) is now integrated between 0 and an arbitrary wall-normal location h in the free stream, i.e., where F'=1, F''=0, to find:

$$\frac{h^2}{2}\left.\frac{\partial \hat{u}_{0,0}}{\partial \eta}\right|_{\eta=0} = \int_0^h \hat{u}_{0,0}\mathrm{d}\eta - 2\bar{x}r_t\int_0^h\int_0^\eta \widehat{\bar{u}\bar{v}}|_{0,0}\mathrm{d}\eta\mathrm{d}\eta + \int_0^h\int_0^\eta\int_0^\eta \mathcal{I}(\bar{x},\eta)\mathrm{d}\eta\mathrm{d}\eta\mathrm{d}\eta. \tag{A.3}$$

By integrating by parts the last two terms on the l.h.s., equation (A.3) is recast into:

$$\left.\frac{\partial \hat{u}_{0,0}}{\partial \eta}\right|_{\eta=0} = \frac{2}{h^2}\int_0^h \hat{u}_{0,0}\mathrm{d}\eta + \frac{4\bar{x}r_t}{h^2}\int_0^h (\eta-h)\widehat{\bar{u}\bar{v}}|_{0,0}\mathrm{d}\eta + \frac{1}{h^2}\int_0^h (\eta-h)^2\mathcal{I}(\bar{x},\eta)\mathrm{d}\eta. \tag{A.4}$$

It is clear that, although h is present on the right-hand side (r.h.s.) of (A.4) the wall-shear stress on the l.h.s. does not depend on h. Therefore, it is convenient to eliminate h from equation (A.4) by taking the limit $h\to\infty$. The first term on the r.h.s. of (A.4), related to the mean-flow distortion $\hat{u}_{0,0}$, and the second term on the r.h.s., containing the Reynolds stress $\widehat{\bar{u}\bar{v}}|_{0,0}$, vanish. The last term on the r.h.s. simplifies as the kernel term $(\eta-h)^2$ disappears. The following expression for the wall-shear stress is thus obtained:

$$\left.\frac{\partial \hat{u}_{0,0}}{\partial \eta}\right|_{\eta=0} = \int_0^\infty \left[\eta F''\hat{u}_{0,0} - 2\bar{x}F'\frac{\partial \hat{u}_{0,0}}{\partial \bar{x}} + F\frac{\partial \hat{u}_{0,0}}{\partial \eta} - 2\bar{x}F''\hat{v}_{0,0} - 2r_t\bar{x}\left.\frac{\partial \widehat{\bar{u}\bar{u}}}{\partial \bar{x}}\right|_{0,0} + r_t\eta\left.\frac{\partial \widehat{\bar{u}\bar{u}}}{\partial \eta}\right|_{0,0}\right]\mathrm{d}\eta. \tag{A.5}$$

The third and last terms on the r.h.s. of (A.5) are further simplified by using integration by parts and the no-slip and far-field boundary conditions to obtain the final integral expression (15).

It is worth remarking that the final expression (15) is valid for either uncontrolled or wall-transpiration cases. In the original FIK identity for the case of turbulent channel flow with uniform suction on one wall and uniform blowing on the other wall (equation (16) in Fukagata et al. [19]), the y-independent transpiration velocity appears explicitly outside of the second integral in order to single out the effect of this quantity. In our case the averaged quantity $\hat{v}_{0,0}$ depends on η and therefore it is not convenient to decompose the $\bar{v}$ velocity of the Reynolds stresses on the r.h.s. of (A.4) into the sum of $\hat{v}_{0,0}$ and the fluctuating component, as performed in Fukagata et al. [19], because $\hat{v}_{0,0}$ could not be moved outside of the integral. However, this point only applies to expression (A.4) and not to the simpler final relation (15) because, as proved by taking the limit h *rightarrow*∞ in (A.4), the Reynolds stresses $\widehat{\bar{u}\bar{v}}|_{0,0}$ are not present in the final expression (15).

The Reynolds stresses instead play a crucial role in the identities for confined turbulent channel flows and open free-stream turbulent boundary layers, derived in the original FIK publication[19]. The integral equation for open turbulent boundary layers derived by Fukagata et al. [19] does contain the term proportional to the Reynolds stresses

because the upper limit of the wall-normal integration is fixed, i.e., it is the boundary-layer thickness. It is therefore in a form analogous to our relation (A.4), where h appears explicitly and the Reynolds stresses are present in the second term on the r.h.s.

---

[1] Balakumar, P., Hall, P., 1999. Optimum suction distribution for transition control. Theor. Comp. Fluid Dyn. 13, 1–19.

[2] Bassom, A., Hall, P., 1994. The receptivity problem for O(1) wavelength Görtler vortices. Proc. R. Soc. Lond. A 446 (1928), 499–516.

[3] Benmalek, A., Saric, W., 1994. Effects of curvature variations on the nonlinear evolution of Görtler vortices. Phys. Fluids 6 (10), 3353–3367.

[4] Bertolotti, F., 1993. Vortex generation and wave-vortex interaction over a concave plate with roughness and suction. ICASE, 93–101.

[5] Bippes, H., Görtler, H., 1972. Dreidimensionale störungen in der grenzschicht an einer konkaven wand. Acta Mechanica 14 (4), 251–267.

[6] Bodonyi, R., Duck, P., 1990. Boundary-layer receptivity due to a wall suction and control of Tollmien-Schlichting waves. Tech. rep., NASA Contractor Report 182103, ICASE Report No. 90-62.

[7] Boiko, A., Ivanov, A., Kachanov, Y., Mischenko, D., 2010. Steady and unsteady Görtler boundary-layer instability on concave wall. Europ. J. Mech. B/Fluids 29 (2), 61–83.

[8] Brown, A., Martin, B., 1982. Flow transition phenomena and heat transfer over the pressure surfaces of gas turbine blades. J. Eng. Power Trans. ASME 104 (2), 360–367.

[9] Canuto, C., Hussaini, M., Quarteroni, A., Zang, T., 1988. Spectral Methods in Fluid Dynamics. Springer-Verlag, New York.

[10] Cathalifaud, P., Luchini, P., 2000. Algebraic growth in boundary layers: optimal control by blowing and suction at the wall. Eur. J. Mech. - B Fluids 19, 469–490.

[11] Cossu, C., Chomaz, J.-M., Huerre, P., Costa, M., 2000. Maximum spatial growth of Görtler vortices. Flow, Turb. and Comb. 65 (3-4), 369–392.

[12] De Souza, L., de Mendonça, M., De Medeiros, M., Kloker, M., 2004. Seeding of Görtler vortices through a suction and blowing strip. J. Braz. Soc. Mech. Sci. Eng. 26 (3), 269–279.

[13] Denier, J., Hall, P., Seddougui, S., 1991. On the receptivity problem for Görtler vortices: vortex motions induced by wall roughness. Phil. Trans. R. Soc. Lond. A 335 (1636), 51–85.

[14] Dongdong, X., Zhang, Y., Wu, X., 2017. Nonlinear evolution and secondary instability of steady and unsteady Görtler vortices induced by free-stream vortical disturbances. J. Fluid Mech. 829, 681–730.

[15] Dongdong, X., Zhang, Y., Wu, X., 2017. Nonlinear evolution and secondary instability of steady Görtler vortices induced by free-stream vortical disturbances. In: 47th AIAA Fluid Dynamics Conf. p. 3459.

[16] Finnis, M., Brown, A., 1997. The linear growth of Görtler vortices. Int. J. Heat and Fluid Flow 18 (4), 389–399.

[17] Floryan, J., Saric, W., 1982. Stability of Görtler vortices in boundary layers. AIAA J. 20 (3), 316–324.

[18] Floryan, J., Saric, W., 1983. Effects of suction on the Görtler instability of boundary layers. AIAA J. 21, 1635–1639.

[19] Fukagata, K., Iwamoto, K., Kasagi, N., 2002. Contribution of Reynolds stress distribution to the skin friction in wall-bounded flows. Phys. Fluids 14 (11), 73–76.

[20] Hall, P., 1982. On the non-linear evolution of Görtler vortices in non-parallel boundary layers. IMA J. Appl. Math. 29 (2), 173–196.

[21] Hall, P., 1983. The linear development of Görtler vortices in growing boundary layers. J. Fluid Mech. 130, 41–58.

[22] Hall, P., 1988. The nonlinear development of Görtler vortices in growing boundary layers. J. Fluid Mech. 193, 243–266.

[23] Hall, P., 1990. Görtler vortices in growing boundary layers: the leading edge receptivity problem, linear growth and the nonlinear breakdown stage. Mathematika 37 (74), 151–189.

[24] Hall, P., Horseman, N. J., 1991. The linear inviscid secondary instability of longitudinal vortex structures in boundary layers. J. Fluid Mech. 232, 357–375.

[25] Joslin, R., 1998. Aircraft laminar flow control. Ann. Rev. Fluid Mech. 30, 1–29.

[26] Kim, J., Simon, T., Russ, S., 1992. Free-stream turbulence and concave curvature effects on heated, transitional boundary layers. J. Heat Transfer 114 (2), 338–347.

[27] Kottke, V., 1988. On the instability of laminar boundary layers along concave walls towards Görtler vortices. In: Propagation in Systems Far from Equilibrium. Springer, pp. 390–398.

[28] Leib, S., Wundrow, D., Goldstein, M., 1999. Effect of free-stream turbulence and other vortical disturbances on a laminar boundary layer. J. Fluid Mech. 380, 169–203.

[29] Li, F., Malik, M., 1995. Fundamental and subharmonic secondary instabilities of Görtler vortices. J. Fluid Mech. 297, 77–100.

[30] Luchini, P., Bottaro, A., 1998. Görtler vortices: a backward-in-time approach to the receptivity problem. J. Fluid Mech. 363, 1–23.

[31] Mangalam, S., Dagenhart, J., Hepner, T., Meyers, J., 1985. The Görtler instability on an airfoil. AIAA Paper 85-0491.

[32] Marensi, E., 2016. Nonlinear unsteady disturbances generated by the interaction of free-stream vorticity with a laminar boundary layer. Ph.D. thesis, University of Sheffield.

[33] Myose, R., Blackwelder, R., 1995. Control of streamwise vortices using selective suction. AIAA J. 33 (6), 1076–1080.
[34] Papadakis, G., Lu, L., Ricco, P., 2016. Closed-loop control of boundary layer streaks induced by free-stream turbulence. Phys. Rev. Fluids 1 (4), 043501.
[35] Peerhossaini, H., Bahri, F., 1998. On the spectral distribution of the modes in nonlinear Görtler instability. Exp. Therm. Fluid Sci. 16 (3), 195–208.
[36] Pope, S., 2000. Turbulent Flows. Cambridge University Press.
[37] Pozrikidis, C., 1998. Numerical computation in science and engineering. Vol. 6. Oxford University press New York.
[38] Ricco, P., 2006. Response of a compressible laminar boundary layer to free-stream turbulence. PhD Thesis, University of London.
[39] Ricco, P., Dilib, F., 2010. The influence of wall suction and blowing on laminar boundary-layer streaks generated by free-stream vortical disturbances. Phys. Fluids 22 (044101).
[40] Ricco, P., Luo, J., Wu, X., 2011. Evolution and instability of unsteady nonlinear streaks generated by free-stream vortical disturbances. J. Fluid Mech. 677, 1–38.
[41] Ricco, P., Shah, D., Hicks, P., 2013. Compressible laminar streaks with wall suction. Phys. Fluids 25 (054110).
[42] Ricco, P., Walsh, E., Brighenti, F., McEligot, D., 2016. Growth of boundary-layer streaks due to free-stream turbulence. Int. J. Heat Fluid Flow 61, 272–283.
[43] Saric, W., 1994. Görtler vortices. Annu. Rev. Fluid Mech. 26 (1), 379–409.
[44] Saric, W., Carrillo Jr, R., Reibert, M., 1998. Leading-edge roughness as a transition control mechanism. In: 36th AIAA Aerospace Sciences Meeting and Exhibit. Vol. 98-0781.
[45] Saric, W., Carrillo Jr, R., Reibert, M., 1998. Nonlinear stability and transition in 3-D boundary layers. Meccanica 33 (5), 469–487.
[46] Schrader, L.-U., Brandt, L., Zaki, T., 2011. Receptivity, instability and breakdown of Görtler flow. J. Fluid Mech. 682, 362–396.
[47] Schultz, M., Volino, R., 2003. Effects of concave curvature on boundary layer transition under high freestream turbulence conditions. J. Fluids Eng. 125 (1), 18–27.
[48] Sescu, A., Yassir, S., Visbal, M., 2016. Compressible boundary layer receptivity to free-stream disturbances and step excrescences. In: 46th AIAA Fluid Dynamics Conference. pp. 1–23.
[49] Souza, L., 2017. On the odd and even secondary instabilities of Görtler vortices. Theor. Comput. Fluid Dyn., 1–21.
[50] Swearingen, J., Blackwelder, R., 1983. Parameters controlling the spacing of streamwise vortices on concave walls. AIAA Paper (83-0380).
[51] Swearingen, J., Blackwelder, R., 1987. The growth and breakdown of streamwise vortices in the presence of a wall. J. Fluid Mech. 182, 255–290.
[52] Tandiono, T., Winoto, S., Shah, D., 2008. On the linear and nonlinear development of Görtler vortices. Phys. Fluids 20 (9), 094103.
[53] Tandiono, T., Winoto, S., Shah, D., 2013. Spanwise velocity component in nonlinear region of Görtler vortices. Phys. Fluids 25 (10), 104104.
[54] Volino, R., Simon, T., 1995. Bypass transition in boundary layers including curvature and favorable pressure gradient effects. J. Turbomach. 117 (1), 166–174.
[55] Wassermann, P., Kloker, M., 2002. Mechanisms and passive control of crossflow-vortex-induced transition in a three-dimensional boundary layer. J. Fluid Mech. 456, 49–84.
[56] Wu, X., Jacobs, R., Hunt, J., Durbin, P., 1999. Simulation of boundary layer transition induced by periodically passing wakes. J. Fluid Mech. 398, 109–153.
[57] Wu, X., Zhao, D., Luo, J., 2011. Excitation of steady and unsteady Görtler vortices by free-stream vortical disturbances. J. Fluid Mech. 682, 66–100.
[58] Wundrow, D., Goldstein, M., 2001. Effect on a laminar boundary layer of small-amplitude streamwise vorticity in the upstream flow. J. Fluid Mech. 426, 229–262.
[59] Yoshioka, S., Fransson, J., Alfredsson, P., 2004. Free stream turbulence induced disturbances in boundary layers with wall suction. Phys. Fluids 16 (10), 3530–3539.
[60] Zhang, Y., Zaki, T., Sherwin, S., Wu, X., 2011. Nonlinear response of a laminar boundary layer to isotropic and spanwise localized free-stream turbulence. In: The 6th AIAA Theoretical Fluid Mechanics Conference. Vol. 3292.